Magnetic Resonance in Medicine

WILEY | ISMRM ONE COMMUNITY FOR CLINICIANS AND SCIENTISTS

RESEARCH ARTICLE OPEN ACCESS

Modelling Motion-Induced Signal Corruption in Steady-State Diffusion MRI

Benjamin C. Tendler | Wenchuan Wu | Karla L. Miller | Aaron T. Hess

Centre for Integrative Neuroimaging, FMRIB, Nuffield Department of Clinical Neurosciences, University of Oxford, Oxford, UK

Correspondence: Benjamin C. Tendler (benjamin.tendler@ndcn.ox.ac.uk)

Received: 28 August 2025 | **Revised:** 10 February 2026 | **Accepted:** 12 February 2026

Keywords: diffusion MRI | diffusion-weighted steady-state free precession | extended phase graphs | in vivo | motion correction | steady-state diffusion

ABSTRACT

Purpose: Diffusion-weighted steady-state free precession (DW-SSFP) is a diffusion imaging sequence achieving high SNR efficiency. A key challenge for in vivo DW-SSFP is the sequence's severe motion sensitivity, currently limiting investigations to low or no motion regimes. Here we establish a framework to both (1) model and (2) correct for the impact of subject motion associated with the underlying magnetisation distribution of DW-SSFP.

Theory and Methods: An extended phase graphs (EPG) representation of the 1D DW-SSFP signal was established incorporating a motion operator describing rigid body and pulsatile motion. The representation was validated using Monte Carlo simulations, and subsequently integrated into a data fitting routine for motion estimation and correction. The fitting routine was evaluated using both simulations and a voxelwise correction applied to in vivo experimental 2D low-resolution single-shot timeseries DW-SSFP data acquired in the human brain in three healthy volunteers, with a tensor reconstructed from the motion-corrected experimental DW-SSFP data.

Results: The proposed EPG-motion framework gives excellent agreement to complementary Monte Carlo simulations, demonstrating that diffusion coefficient estimation is robust over a range of motion and SNR regimes. Tensor estimates from the motion-corrected experimental DW-SSFP data give good visual agreement to complementary diffusion-weighted spin-echo (DW-SE) data acquired in the same subject, considerably reducing orientation-dependent motion-induced biases.

Conclusion: Temporal information capturing the evolution of the DW-SSFP signal can be used to retrospectively (1) estimate subject motion and (2) reconstruct motion-corrected DW-SSFP data. Open-source software is provided, facilitating future investigations into the impact of subject-motion on DW-SSFP acquisitions.

1 | Introduction

In diffusion MRI, applied diffusion encoding gradients sensitise signals to the microscopic (μm) scale, with diffusion processes in tissue leading to attenuation of signal magnitude [1]. Measured signals are also intrinsically sensitive to subject motion, with small tissue displacements (e.g., arising from bulk, pulsatile, or respiratory induced motion) leading to changes in signal phase [2, 3]. The presence of motion-induced artefacts in reconstructed images is strongly dependent on the incorporated readout scheme. The combination of phase-inconsistent k-space data associated with segmented readouts can give rise to considerable artefacts in reconstructed magnitude images [4], impacting the quantification of diffusion attenuation. Diffusion-weighted spin-echo (DW-SE) [1] sequences incorporating single-shot readouts are typically considered motion robust [5, 6], with a notable

exception of motion induced 'dropout' arising when the echo is displaced from the k-space field of view (FOV) [7–9].

Diffusion-weighted steady-state free precession (DW-SSFP) [10–13] is an alternative to the DW-SE for diffusion MRI investigations. DW-SSFP is typically implemented as a 3D sequence, with a diffusion encoding module consisting of a single diffusion gradient and RF pulse per TR (Figure 1). The signal-forming mechanisms of DW-SSFP have previously demonstrated high-SNR efficiency [16, 17], with the sequences' short TR (~20 to 40 ms) compatible with a segmented readout acquiring a single line (or a few lines) of k-space per TR, leading to images with minimal geometric distortions. Whilst offering considerable potential for in vivo investigations, previous work has demonstrated that the DW-SSFP acquisitions are highly sensitive to both rigid body (head translation/rotation) and pulsatile (i.e., arising from the cardiac cycle) motion [18–23]. At present, the motion-sensitivity of DW-SSFP limits investigations to low (cartilage [17, 24], peripheral nerves [25]) or no (post-mortem [16]) motion imaging regimes.

Several motion-correction methods have been previously established to address motion artefacts arising from segmented diffusion MRI acquisitions. Typically, these methods introduce navigator echoes [26, 27] or 'self-navigating' readouts (e.g., PROPELLER [28, 29], SNAILS [30, 31]) to the sequence, or exploit sensitivity encodings (e.g., MUSE [32], MUSSELS [33]) to estimate and correct for motion-induced phase inconsistencies across acquired k-space segments. These techniques have demonstrated considerable promise for the DW-SE sequence, raising a simple question—can we directly translate an existing method to correct for subject motion in DW-SSFP?

Unfortunately, a key challenge for DW-SSFP is the specialised nature of how motion corrupts the signal associated with the underlying magnetisation distribution (i.e., independent of the readout scheme and k-space coverage). Specifically, whilst subject motion corrupts the DW-SE signal phase, in DW-SSFP subject motion corrupts both the signal phase *and* magnitude [3] and persists over many TRs (Figure 2). Whilst conventional motion-correction techniques can be incorporated to attenuate artefacts associated with the sequence's segmented readout [18–22], we require further extensions to account for the signal forming mechanisms of DW-SSFP.

Specifically, as DW-SSFP is a steady-state sequence, magnetisation excited in a single TR persists and evolves over multiple TRs. Over time the DW-SSFP signal reaches a steady-state (Figure 2), with the signal reflecting a weighted sum of magnetisation components with different evolution histories. Motion at any timepoint leads to phase corruption of the excited magnetisation, which over future TRs will combine with magnetisation components with different motion histories and associated phase corruption, leading to phase cancellation and subsequent magnitude loss (Figure 2). This includes the combination of phase corrupted magnetisation with 'fresh' magnetisation (i.e., longitudinally recovered magnetisation that has been excited into the transverse plane) that has no motion history. This form of magnitude loss is independent of the readout scheme and k-space coverage. From the perspective of Extended Phase Graphs [35] (EPG), magnitude corruption of the DW-SSFP signal arises from

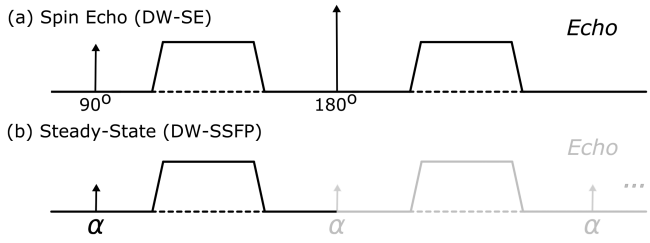

FIGURE 1 | Diffusion encoding. Diffusion encoding modules of the (a) diffusion-weighted spin-echo (DW-SE) and (b) diffusion-weighted steady-state free precession (DW-SSFP) sequence. DW-SSFP consists of a single RF pulse and diffusion gradient per TR (typically 20–40 ms). Magnetisation accumulates diffusion contrast over several TRs, consistent with dephasing and rephasing of magnetisation due to gradient pairs in the DW-SE. The steady-state DW-SSFP signal (reached after many TRs) can be considered a superposition of multiple magnetisation components with different histories—for example, pairs of diffusion-weighted gradients separated by a variable integer number of TRs that lead to different degrees of diffusion weighting. The measured signal is the sum of these different magnetisation components, with diffusion-weighting dependent on the applied diffusion gradient, TR, flip angle, T_1, T_2 and diffusion coefficient [14, 15].

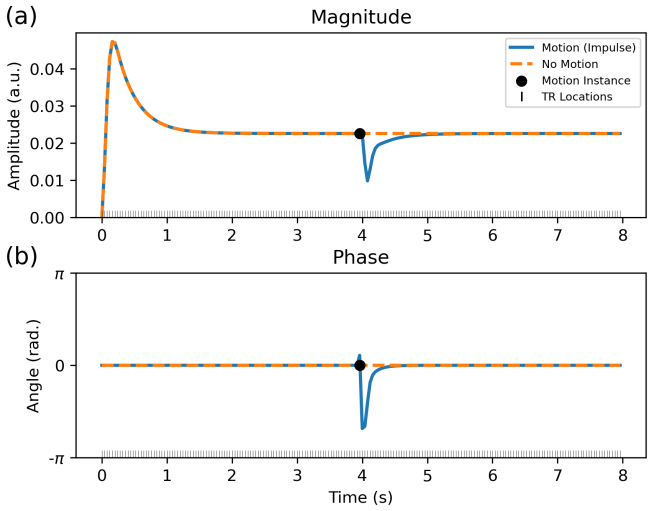

FIGURE 2 | DW-SSFP signal evolution with impulse motion. Simulated 1D time-series profile of the DW-SSFP (a) magnitude and (b) phase signal over 200 TRs. After ~50 TRs (2 s), the signal reaches a steady state. Impulse motion simulated during a single TR (black dot) perturbs the steady state. This motion-corrupted magnetisation persists and contributes to future TRs, leading to a slow recovery to the original steady state, with both the magnitude and phase signal impacted. Sequence parameters based on the experimental investigation performed in Miller and Pauly [19], setting $G = 40$ mT/m, $\delta = 6.5$ ms, $\alpha = 30^o$, TR = 40 ms and $\phi = 0^o$. Impulse motion was modelled using a velocity of 1.5 mm/s along the diffusion gradient orientation during a single TR (40 ms) using the proposed EPG-motion framework (see Section 2), leading to a total displacement of 0.06 mm. Sample parameters based on approximate in vivo values in brain tissue at 3T [34], defining $D = 1 \cdot 10^{-3}$ mm^2/s, $T_1 =$ 832 ms and $T_2 = 110$ ms.

the combination of magnetisation pathways with different phase values during the evolution of the phase graph.

Several methods have been proposed to address motion artefacts in DW-SSFP [18–22], generally by adopting navigator-based phase corrections that were originally proposed for DW-SE. A key limitation of these previous methods is that they do not account for the loss of signal magnitude arising from the combination of magnetisation components with different evolution histories, leading to residual artefacts in reconstructed images. One notable exception is work by O'Halloran et al. [23] establishing a prospective motion-correction method for DW-SSFP utilising real-time information to estimate and correct for deviations in image phase arising from rigid-body motion of the subject, providing partial attenuation of magnitude signal loss.

In this work, we perform a theoretical investigation, and experimental validation, into the impact of subject motion on the DW-SSFP signal associated with the underlying magnetisation distribution (i.e., independent of the readout and k-space coverage). We demonstrate that the loss of motion-induced signal magnitude associated with the magnetisation distribution can be estimated and corrected *retrospectively* using timeseries data capturing the evolution of the DW-SSFP signal. To achieve this, we first introduce a theoretical framework based on EPG [35] (building on a previous abstract [36]) to characterise how the 1D DW-SSFP signal is corrupted by motion arising from (1) rigid-body motion and (2) brain pulsatility associated with the cardiac cycle. We validate the proposed framework using Monte Carlo simulations and use the framework to visualise how changes in the magnetisation distribution arising from subject motion impacts DW-SSFP data. We demonstrate that motion-corrupted DW-SSFP data can contain sufficient information to estimate and reconstruct motion-corrected estimates, evaluating the framework experimentally by applying a voxel-wise correction to in vivo 2D low-resolution single-shot DW-SSFP timeseries data acquired in the human brain.

Our work addresses a specific sub-problem of motion corruption arising from the magnetisation distribution of DW-SSFP under the assumption of an instantaneous readout (i.e., all k-space data required to form an image is acquired in a single TR, here approximated experimentally using a single-shot readout). The proposed model forms the foundation for future DW-SSFP motion-correction methods incorporating information about the k-space readout and coverage, required for translation to a conventional 3D multi-shot DW-SSFP acquisition. Open-source software is provided to enable researchers to replicate many of the findings in this manuscript and perform their own investigations on the impact of subject motion on DW-SSFP data (github.com/BenjaminTendler/MotionCorrectionDWSSFP).

2 | Theory

2.1 | Extended Phase Graphs (EPG)

In this work, we use EPG to characterise the impact of motion on the DW-SSFP signal. Briefly, EPG describes a widely adopted framework for modelling the magnetisation evolution of an MRI sequence. It provides a solution to the Bloch equations [37], reparameterising magnetisation as a Fourier basis with distinct phase states of dephasing order k, defining:

- Longitudinal ($\tilde{Z}$) and transverse ($\tilde{F}$) magnetisation components with different k states ($\tilde{Z}_k$, $\tilde{F}_k$).
- RF pulses acting as an operator that mixes $\tilde{Z}_k$ and $\tilde{F}_k$ components of a given k.
- Magnetic field gradients acting on $\tilde{F}_k$ components by increasing or decreasing their dephasing order.

EPG describes the magnetisation evolution in each TR as a series of steps. An RF pulse operator first mixes $\tilde{Z}_k$ and $\tilde{F}_k$ components, followed by the application of additional operators (describing relaxation, motion, diffusion, etc.) during the TR, with the dephasing order (k) of magnetisation components updated based on the applied magnetic field gradients. Mathematically, the EPG framework formalises magnetisation components as 3×1 vectors of $\tilde{F}_k$ and $\tilde{Z}_k$ states, acted on by 3×3 operator matrices. For readers unfamiliar with EPG signal representations, we recommend the review article by Weigel [35].

2.2 | Extended Phase Graphs and Diffusion

The impact of diffusion attenuation has been previously incorporated into an EPG framework via a diffusion operator [38], $\mathbf{D}$. For a periodic sequence, in which each TR contains a diffusion gradient of duration δ, $\mathbf{D}$ is given by:

$$\mathbf{D} = \begin{bmatrix} e^{-\left(\left(k_1+\frac{\Delta k}{2}\right)^2+\frac{\Delta k^2}{12}\right)\cdot\delta\cdot \mathrm{D}} \cdot e^{-k_2^2\cdot(\mathrm{TR}-\delta)\cdot \mathrm{D}} & 0 & 0 \\ 0 & e^{-\left(\left(k_1+\frac{\Delta k}{2}\right)^2+\frac{\Delta k^2}{12}\right)\cdot\delta\cdot \mathrm{D}} \cdot e^{-k_2^2\cdot(\mathrm{TR}-\delta)\cdot \mathrm{D}} & 0 \\ 0 & 0 & e^{-k_1^2\cdot \mathrm{TR}\cdot \mathrm{D}} \end{bmatrix}, \quad (1)$$

where $k_1$and k_2 are the dephasing order before and after application of the diffusion gradient, $\Delta k = k_2 - k_1$, and D is the diffusion coefficient. When considering diffusion gradients, we can define the dephasing order as an integer multiple of the diffusion gradient's q-value, $q = \int \gamma \cdot G(t) \cdot dt$, with the change in dephasing order during the application of a diffusion gradient equivalent to $\Delta k = q$.

The product of the two exponentials present in matrix elements $\mathbf{D}_{1,1}$ and $\mathbf{D}_{2,2}$ characterises the diffusion attenuation associated with transverse magnetisation during (1) the application of a diffusion gradient of duration δ and (2) the remaining TR period. The exponential at location $\mathbf{D}_{3,3}$ characterises the diffusion attenuation experienced by longitudinal magnetisation in a single TR.

2.3 | Extended Phase Graphs and Motion

Analogous to the description of the diffusion operator in the previous section, we can characterise motion in EPG via a motion operator, **J**.In this work, we extend previous descriptions of **J**[35] to incorporate (1) gradients of fixed duration, (2) subject rotation and (3) time-dependence. Assuming motion as linear (i.e., constant translational/rotational velocity), we can define:

$$\mathbf{J} = \begin{bmatrix} e^{-i\cdot\frac{k_1+k_2}{2}\cdot\delta\cdot V}\cdot e^{-i\cdot k_2\cdot(\mathrm{TR}-\delta)\cdot V} & 0 & 0 \\ 0 & e^{i\cdot\frac{k_1+k_2}{2}\cdot\delta\cdot V}\cdot e^{i\cdot k_2\cdot(\mathrm{TR}-\delta)\cdot V} & 0 \\ 0 & 0 & e^{-i\cdot k_1\cdot\mathrm{TR}\cdot V} \end{bmatrix}, \tag{2}$$

where

$$V = \vec{v}\cdot\hat{g} + (\hat{g}\times\vec{\omega})\cdot\vec{X}, \tag{3}$$

where $\hat{g}$ =unit vector describing gradient orientation, $\vec{v}$ = translational velocity, $\vec{\omega}$ = rotational velocity and $\vec{X}$ = spatial location (relative to the centre of rotation). Equation (2) demonstrates that motion leads to a change in the phase of a magnetisation component, with the polarity of motion (i.e., positive or negative) preserved in the sign of the phase change. To incorporate changes in the motion profile across TRs, we can define:

$$V_n = \vec{v}_n\cdot\hat{g} + \left(\hat{g}\times\vec{\omega}_n\right)\cdot\vec{X}_n, \tag{4}$$

where the subscript indicates the parameters for the nth TR, and V_n is a scalar constant representing the component of instantaneous velocity along the orientation of the diffusion gradient during a given TR. We subsequently refer to the evolution of V_n across multiple TRs as $V(t)$.

The steady-state diffusion signal persists for several seconds over multiple TRs, with the signal lifetime dictated primarily by T_1. When considering forms of motion that are dependent on the spatial location $\vec{X}$ (e.g., rotations), the motion operator must account for cumulative changes in $\vec{X}$ over the time-course of an acquisition. Assuming a single time-step per TR, we define:

$$\vec{X}_{n+1} = \boldsymbol{R}\left(\vec{\theta}_n\right)\vec{X}_n + \vec{x}_n, \tag{5}$$

where $\boldsymbol{R}(\vec{\theta})$ is a 3D rotation matrix operation = $\boldsymbol{R_z}(\theta_z)\boldsymbol{R_y}(\theta_y)\boldsymbol{R_x}(\theta_x)$, $\vec{\theta}_n = \vec{\omega}_n\cdot\mathrm{TR}$ and $\vec{x}_n = \vec{v}_n\cdot\mathrm{TR}$. We note that the proposed motion operator is not specific to DW-SSFP and could be incorporated into EPG schemes investigating the impact of motion on arbitrary MRI sequences, including diffusion-weighted double-echo steady-state (DW-DESS) [39–41] and MR fingerprinting [42, 43] methods.

As implied from Equation (3), only velocity components parallel to the applied diffusion gradient $\hat{g}$ contribute to the motion operator in Equation (2) and lead to a motion-induced signal change. As the velocity profile of rigid body and pulsatile motion in the brain are orientation dependent, DW-SSFP data acquired with different diffusion gradient orientations will be associated with different motion profiles, leading to signal corruption beyond a global loss of SNR. Beyond orientation effects, the degree of signal corruption is dependent on the properties of the diffusion-encoding scheme and the evolution of the motion profile over time (Equation 4).

Figure 3 compares a simulated time-series evolution of the DW-SSFP signal using (1) EPG integrating the proposed motion operator and (2) Monte Carlo simulations (see Section 3) for fixed rigid-body motion (left column) and a temporally varying motion profile characterising cardiac pulsatility (right column). Excellent agreement is found between the two approaches. Notably, motion in the EPG implementation was modelled using a single timestep per TR (Equation 4), with motion in the Monte Carlo implementation modelled using 100 timesteps per TR. Agreement between the two approaches suggests that the short TR of DW-SSFP enables motion to be captured as a single parameter in each TR.

2.4 | Motion Induced Image Corruption in DW-SSFP

To visualise the impact of motion on DW-SSFP images, we can utilise the proposed EPG-motion framework to simulate the signal evolution of individual voxels in a DW-SSFP data set. Figure 4a–d displays synthesised DW-SSFP images assuming an instantaneous single-shot readout incorporating (a) no motion, (b) translation along a single dimension, (c) rotation along a single dimension and (d) cardiac pulsatility. Here we observe that even simple forms of rigid-body motion lead to complicated spatial changes in both signal magnitude and phase. Signal changes arising from pulsatile motion (Figure 4d) give good visual agreement to loss of signal magnitude observed previously [19, 22], with artefacts propagating into images synthesised by simulating a segmented readout (Figure 4e). Comparisons with DW-SE images acquired with the same motion profile and an instantaneous readout are displayed in Figure S3, where only changes in the spatial phase profile are observed.

In addition to the loss of signal magnitude in motion-corrupted DW-SSFP data, resulting phase images display local tissue-type contrast (e.g., delineation of CSF filled regions, light orange arrows in Figure 4b) that are not observed in motion-corrupted DW-SE data (i.e., the flat phase maps in Figure S3). This local contrast reflects the interplay between motion and the local diffusion coefficient. In the context of EPG, an increased diffusion coefficient rapidly attenuates the relative contribution of signal forming pathways associated with strong diffusion-weighting, analogous to reducing the relative contribution of signal forming pathways associated with greater motion-corruption (Figure S4). The local diffusion coefficient, D, must therefore be estimated as part of the motion-reconstruction procedure.

The DW-SSFP signal has known dependencies on local tissue relaxation properties (T_1 and T_2) and B_1 [14], which must also be estimated (via complementary mapping techniques) for accurate diffusion and motion modelling. From the perspective of EPG, this property arises as T_1, T_2 and B_1 values additionally modulate the relative contribution of different DW-SSFP signal-forming magnetisation pathways and interact with their relative motion sensitivity, analogous to the description of diffusion coefficients in the previous paragraph. T_1, T_2 and B_1 mapping procedures using complementary imaging sequences have formed a routine part of many DW-SSFP studies estimating quantitative diffusion parameters, with a similar approach used in this study (see Section 3).

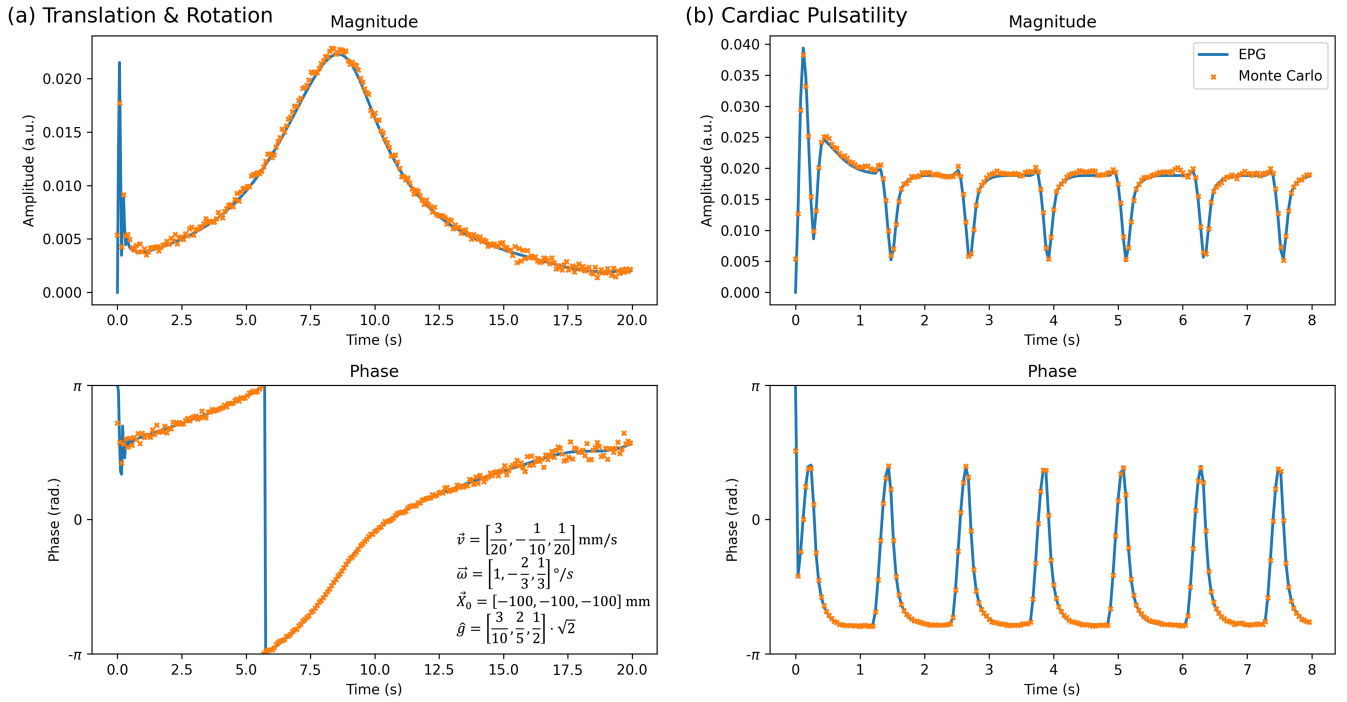

FIGURE 3 | Comparing the EPG-motion operator with Monte Carlo simulations. Motion-corrupted DW-SSFP time-series data simulated using the proposed EPG-motion operator (blue) and Monte Carlo (orange) simulations (see Section 3) for (a) fixed rigid body translation/rotation across all three dimensions and (b) cardiac pulsatility. Rigid body motion parameters associated with Equations (3–5) are displayed in (a). Pulsatility velocity profile (Figure S1) based visually on Greitz et al. [44], simulated defining the maximum pulsatility velocity $\vec{v}_{\text{Card}} = [0, 0, 0.4]$ mm/s and $\hat{g} = [0, 0, 1]$, with total displacement (i.e., integral of the velocity profile) across a single cardiac cycle set equal to zero. Yellow dots correspond to the Monte-Carlo signal estimates at the end of each TR. Sequence parameters based on the experimental investigation performed in Miller and Pauly [19], setting $G =$ 40 mT/m, $\delta = 6.5$ ms, $\alpha = 30^{\text{o}}$, TR = 40 ms and $\phi = 0^{\text{o}}$. Sample parameters were based on approximate in vivo values in brain tissue at $3T$ [34], defining $D = 1 \cdot 10^{-3}$ mm^2/s, $T_1 = 832$ ms and $T_2 = 110$ ms.

2.5 | Does the DW-SSFP Signal Contain Sufficient Information to Reconstruct Motion-Free Estimates?

Earlier in this manuscript, we proposed an EPG operator for motion characterisation (Equation 2), validated using Monte Carlo simulations (Figure 3). Equations (2–4) describe motion in DW-SSFP as fully characterised provided one has knowledge of evolution of V_n across TRs, $V(t)$ (Equation 4). Importantly, whilst individual EPG pathways are associated with different levels of motion corruption in each TR, this difference solely arises from the interplay of $V(t)$ with a pathway's *known* dephasing order, k. This raises the question of whether DW-SSFP data can contain sufficient information to simultaneously estimate $V(t)$ as part of the signal characterisation to reconstruct motion-corrected images. The remainder of the manuscript investigates this using both synthetic and experimental data.

3 | Methods

3.1 | EPG-Motion Framework

Software for simulating (1) $V(t)$ and (2) the DW-SSFP signal incorporating the impact of subject motion was implemented in Python (3.13.2). The provided software allows the modelling of voxelwise and imaging timeseries DW-SSFP data based on a user-defined set of sequence parameters ($G, \tau, TR, \theta, \phi$) and sample properties (T_1, T_2, D, B_1). When simulating 2D and 3D images (e.g., Figure 4), the software models each voxel as independent (i.e., the voxel location is stationary over the time-course of the simulation).

The software was built using NumPy (2.2.4), accelerated with the Numba compiler (0.61.2). For reference, the time required to synthesise (i.e., forward simulate) an arbitrary V(t) profile and subsequent motion corrupted DW-SSFP signal over 200 TRs is $\sim$ 5 ms (single voxel), $\sim$ 10 s (2D slice) and $\sim$ 10 min (3D volume) on a personal laptop.

3.2 | Monte Carlo Simulations

1D DW-SSFP time-series magnitude and phase signals incorporating rigid body and pulsatile motion were synthesised using Monte Carlo simulations (Figure 3). To simulate diffusion, isochromat trajectories were generated using the Camino *datasynth* function [46], modified to produce trajectories that followed a Gaussian distribution of displacements per timestep (10^5 spins, 100 timesteps per TR). Diffusion was simulated as isotropic with a diffusion coefficient of $D = 1 \cdot 10^{-3}$ mm^2/s (approximating in vivo brain tissue). To simulate motion, the location of individual isochromats was updated per timestep via translational

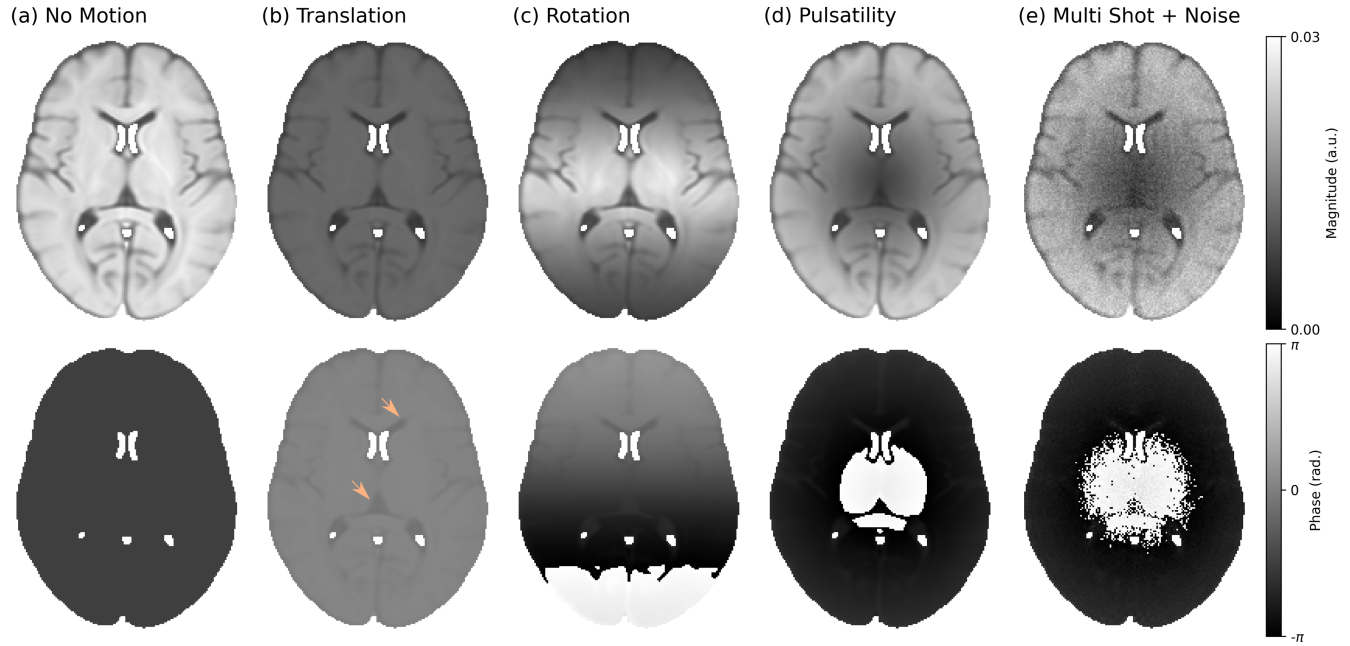

FIGURE 4 | Impact of motion on DW-SSFP images. (a–d) Simulated single-shot DW-SSFP images with an instantaneous readout incorporating (a) no motion (b) constant translation along the foot-head direction ($\vec{v} = [0, 0, 0.2]$ mm/s), (c) constant rotation with the axis of rotation oriented along the left–right direction (i.e., passing through the sagittal plane) ($\vec{\omega} = [0.2, 0, 0]^{o}$/s) and (d) cardiac pulsatility along the foot-head direction ($\vec{v}_{\text{Card}} = [0, 0, 0.4]$ mm/s), all simulated with the diffusion gradient oriented along the foot-head direction ($\hat{g} = [0, 0, 1]$). (e) A simulated DW-SSFP image acquired with a segmented readout (three-line cartesian readout per TR) incorporating cardiac pulsatility only with added Gaussian noise (SNR~20), where each readout is associated with a different component of the cardiac cycle. The light orange arrows overlaid on the phase maps in (b) display local tissue-type contrast reflecting the interplay between motion and the local diffusion coefficient that are not observed in motion-corrupted DW-SE data (Figure S3). Images synthesised using the HCP1065 DTI template mean diffusivity map, available as part of FSL [45]. Pulsatility timeseries profile and relative velocity map based visually on Greitz et al. [44], provided in Figures S1 and S2. Sequence parameters based on the experimental investigation performed in Miller and Pauly [19], setting $G = 40$ mT/m, $\delta = 6.5$ ms, $\alpha = 30^{o}$, TR = 40 ms, $\phi = 0^{o}$. Relaxation parameters (set equal across all voxels) were based on approximate in vivo values in brain tissue at 3T [34], setting $T_1 = 832$ ms and $T_2 = 110$ ms. Images (a–d) are displayed for the 150th TR, corresponding to a simulation duration of 6 s. Image (e) was synthesised using data from the 101st to the 188th TR (ignoring systole), corresponding to an acquisition duration of 3.48 s. Voxels were modelled as independent (i.e., the voxel location is stationary over the time-course of the simulation).

and/or rotational operations using custom software. For the pulsatility simulations, the continuous time-series velocity profile (Figure S1) was averaged across the window associated with each timestep and discretised to define the isochromat displacement.

For the Monte Carlo simulations, the DW-SSFP signal arising from the isochromats was modelled using custom software, implemented in MATLAB (2023a, The MathWorks Inc., Natick, MA). Sequence parameters were based on the experimental investigation performed in Miller and Pauly [19] ($G = 40$ mT/m, $\delta = 6.5$ ms, $\alpha = 30^{o}$, TR $= 40$ ms and RF phase $\phi = 0^{o}$), with relaxation properties based on approximate in vivo values in brain tissue at 3T [34], $T_1 = 832$ ms and $T_2 = 110$ ms.

Monte Carlo simulations incorporating rigid body translational and rotational motion were synthesised defining translational velocity, $\vec{v} = \left[\frac{3}{20}, -\frac{1}{10}, \frac{1}{20}\right]$mm/s, rotational velocity, $\vec{\omega} = \left[1, -\frac{2}{3}, \frac{1}{3}\right]^{\circ}/s$, initial spatial position, $\vec{X}_0 = [-100, -100, -100]$ mm and diffusion gradient orientation, $\hat{g} = \left[\frac{3}{10}, \frac{2}{5}, \frac{1}{2}\right] \cdot \sqrt{2}$. These parameters were chosen to characterise an arbitrary, constant rigid body motion across all three spatial dimensions, achieving large changes in signal magnitude and phase. The pulsatility velocity profile (characterising time-dependent motion) is visualised in Figure S1, setting the maximum pulsatility velocity $\vec{v}_{\text{Card}} = [0, 0, 0.4]$ mm/s and $\hat{g} = [0, 0, 1]$ (i.e., equivalent to the foot-head direction).

3.3 | Parameter Estimation From Simulated DW-SSFP Data (Monte Carlo)

Using the proposed EPG-motion framework, the diffusion coefficient (D), phase offset (ϕ) and V(t) profile were estimated from 1D DW-SSFP timeseries data arising from the Monte Carlo simulations incorporating pulsatility (Figure 3b). The phase offset (ϕ) reflects deviations in the true phase offset versus the defined RF phase angle, equivalent in simulations ($\phi = 0^{o}$) but differing experimentally (arising from spatial B_0 and B_1 profiles). To more accurately reflect experimental conditions, Gaussian noise was added to the simulated signal, leading to a final SNR of 20.

The fitting was implemented in Python (3.13.2) using the Trust Region Reflective algorithm (SciPy *curve_fit* 1.15.2). Specifically, the EPG-motion framework was incorporated as a forward model, with the parameter estimation procedure identifying parameters that minimised the cost function with the

motion-corrupted Monte-Carlo DW-SSFP signal. To accelerate the fitting procedure, an analytical Jacobian function was derived for all parameters (except for the derivative with respect to D, which was estimated numerically). Initialisation parameters and fitting bounds are provided in Table S1, with no additional constraints or regularisation incorporated.

The simulated DW-SSFP timeseries data consisted of 200 TRs. Parameter estimation was performed using a time window of 100 TRs of steady-state signal (after 100 TRs, from 3.96 s in Figure 3b). A single motion parameter was estimated per TR, corresponding to 102 parameters in total ($D + \phi + V(t)$). To facilitate estimation of $V(t)$ the parameter estimation region was split into two components corresponding to (1) dummy measurements (first 25 TRs) and (2) measured signal (remaining 75 TRs). The dummy measurements reflect a series of TRs which were not incorporated into the cost function evaluation. This is important as motion effects build up over several TRs in DW-SSFP. Specifically, the dummy region makes it possible to accurately characterise the motion-corrupted signal from the first TR of the measured signal region by allowing the signal to reach a steady-state incorporating the effects of motion prior to this timepoint. Ten repeats were performed with different noise instances to characterise the robustness of the fitting approach. The fitting procedure averaged at ∼4 s per noise instance (i.e., per 1D timeseries) on a personal laptop (Macbook Pro, Sonoma 14.5, M1, 16GB RAM).

To understand the impact of incorporating motion into the parameter estimation procedure, an identical fitting approach was implemented without estimation of the $V(t)$ operator (i.e., conventional EPG). This corresponds to the estimation of two parameters per simulation ($D + \phi$).

3.4 | Estimation of D as a Function of SNR and Pulsatile Velocity

To assess the robustness of characterising D from motion-corrupted DW-SSFP timeseries data, simulations were performed incorporating pulsatile motion for a range of SNR levels (10, 20, 50, + no noise) and maximum pulsatility velocities (0–1.5 mm/s in 0.3 mm/s increments), where 0 mm/s corresponds to a no motion case and 1.5 mm/s corresponds to a previous experimental estimate of maximum pulsatile velocity in brain tissue [44]. Ten repeats were performed per SNR level and velocity instance (240 simulations total).

3.5 | Experimental Data Acquisition

2D time-series DW-SSFP data were acquired in the brain in three healthy volunteers on a 3T Siemens Prisma scanner (32 channel head coil). Data were acquired in a single axial slice for Subject 1, with axial and coronal slices acquired in Subjects 2 and 3. The subjects gave informed consent with data acquisition in accordance with local ethics committees. Sequence parameters were optimised for a target effective b-value, $b_{\text{eff}} = 500$ s/mm^2, setting $G = 63.6$ mT/m, $\delta = 3.08$ ms, TR = 26 ms, $\alpha = 31^{\circ}$, $\phi = 0^{\circ}$, TE = 15 ms, BW = 2405 Hz/Pix, resolution = $6 \times 6 \times 6$ mm^3, matrix size = 32×32 with a single-shot Cartesian echo planar imaging (EPI) readout (16 msduration). Then, b_0-equivalent data were also acquired with $G = 26.7$ mT/m, producing images that achieve the DW-SSFP spoiling condition with low diffusion weighting ($b_{\text{eff}} = 100$ s/mm^2). These are henceforth referred to as b_{100}, with the $b_{\text{eff}} = 500$ s/mm^2 data referred to as b_{500}.

To ensure the signal reached a steady-state, dummy measurements were performed for 5 s prior to data acquisition. Sequence parameters were chosen via an optimisation routine that maximised SNR-efficiency for the target effective b-value [47]. To evaluate the relationship between the DW-SSFP timeseries data and cardiac pulsatility, pulse oximeter recordings were also acquired.

The time-series data consisted of 384 consecutive measurements in a single axial slice of the brain (10 s acquisition). A fully sampled image was acquired per TR (i.e., equivalent to a 'single-shot' readout) to characterise the temporal dynamics of the DW-SSFP signal independent of a segmented readout scheme. 12 diffusion directions were acquired, with both b_{100} and b_{500} volumes acquired per direction. The raw data (*.dat*) were exported from the scanner and reconstructed using *mapVBVD* [48], with coil-combination performed using SVD and ESPIRiT [49, 50].

The DW-SSFP signal has known dependencies on tissue relaxation (T_1 and T_2) properties and the B_1 profile. Complementary T_1, T_2 and B_1 maps were estimated in the same subject using a spin echo EPI sequence with different inversion preparations (ep2d_se), multi-echo spin-echo (se_mc) and 3DREAM [51]. Full details of the sequence parameters and processing are provided in Table S1.

To facilitate comparisons, 2D DW-SE EPI data were additionally acquired within the same subjects, closely matching the acquisition scheme of the DW-SSFP data (b_0 and $b = 500$ s/mm^2, 12 diffusion directions). Full details of the DW-SE EPI sequence parameters and image processing are provided in Table S1.

3.6 | Parameter Estimation From Experimental DW-SSFP Data

The diffusion coefficient (D), signal amplitude (S_0), phase offset (ϕ) and $V(t)$ operator were estimated from experimental DW-SSFP timeseries data using the proposed EPG-motion framework. The fitting procedure was implemented in Python (3.13.2) as described above, fitting simultaneously to the time-series b_{100} and b_{500} data. Initialisation parameters and fitting bounds are provided in Table S3, with no additional constraints or regularisation incorporated. Fitting was performed independently for each voxel and diffusion direction, estimating a single diffusion coefficient per voxel.

For the fitting procedure, DW-SSFP timeseries data were simulated for 509 TRs. This consisted of 100 TRs to ensure the simulated signal reached a steady-state, 25 TRs dummy measurements and 384 TRs where comparisons were made to the acquired experimental data. A single motion parameter was estimated per TR, corresponding to the estimation of 822 parameters per voxel ($D + S_0 + \phi_{b100} + \phi_{b500} + V_{b100}(t) + V_{b500}(t)$). Parameter estimation required ∼30 s per voxel on a personal laptop (Macbook Pro, Sonoma 14.5, M1, 16GB RAM). Finally, a tensor was

reconstructed from the estimated D maps acquired across all 12 orientations using custom software.

To understand the impact of incorporating motion into the parameter estimation procedure, an identical fitting approach was implemented without estimation of the $V(t)$ operator (i.e., conventional EPG), estimating four parameters per simulation ($D + S_0 + \phi_{b100} + \phi_{b500}$).

4 | Results

Figure 5 displays the estimated DW-SSFP time-series and $V(t)$ operator using the proposed EPG-motion framework, arising from Monte Carlo simulations of the steady-state DW-SSFP signal incorporating pulsatile motion with added Gaussian noise. Excellent agreement is found over the fitted data region (green box), indicating that simultaneous estimation of $V(t)$ and D is possible from DW-SSFP timeseries data.

When considering diffusion MRI acquisitions, the key parameter we want to accurately characterise is the diffusion coefficient, D. By means of comparison, given the simulated coefficient ($D = 1 \cdot 10^{-3}$ mm^2/s), fitting to the simulated data with no estimation of $V(t)$ (i.e., conventional EPG) yielded $D = (2.00 \pm 0.02) \cdot 10^{-3}$ mm^2/s. Fitting with the proposed EPG-motion framework estimated $D = (0.99 \pm 0.04) \cdot 10^{-3}$ mm^2/s.

Data acquisition for a DW-SSFP experiment does not begin at the first TR, with motion during the build-up to a steady state leading to motion corruption of the DW-SSFP signal from the first TR of data acquisition. This is visible in the measured data region of Figure 5 (green box), where the signal amplitude in the first TR is below the amplitude predicted of a motion-free DW-SSFP signal (Figure 5, dashed orange line). If the estimation of motion only begun at the first TR of the measured data region (green box), it would not be possible to accurately estimate the motion profile or the signal in the first few TRs of the measured data region, as it would have to immediately transition from a motion-free steady-state to a measurement representing the evolution of a motion-corrupted DW-SSFP signal that has arisen over several TRs.

To account for this, the parameter estimation routine allows for motion to be incorporated into the TRs prior to the measurement region, here referred to as dummy measurements (pink box). In this box no cost function evaluations are made, with the presence of dummy measurements enabling the signal to be accurately represented from the first TR of the measured data region (green box). The choice of 25 TRs corresponds to a single second of data, reflecting the approximate time required to return to steady state for an instantaneous motion operation (Figure 2) based on the simulated parameters investigated here. The arbitrary evolution of the signal/motion profiles in the dummy measurement region (pink box) arises as no cost-function evaluations are made, meaning parameter estimation is poorly conditioned in this region. However, the signal/motion profiles begin to more closely represent the ground truth as the measured data region is approached (right-hand side of the pink box), with the accurate representation of the motion profile from the first TR of the measured data region (green) demonstrating that their inclusion is working as intended.

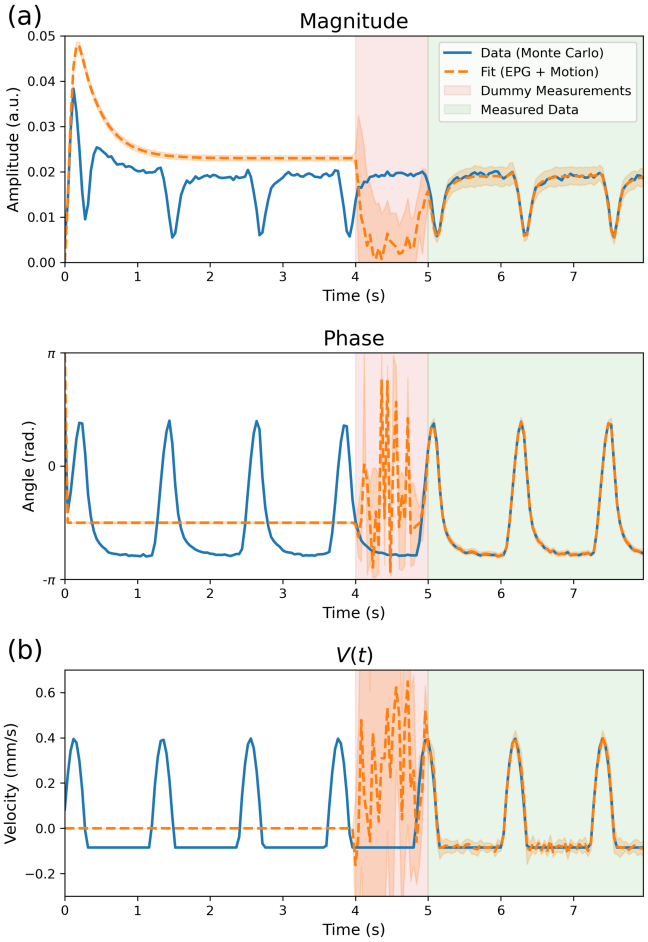

FIGURE 5 | Estimation of $V(t)$ from simulated DW-SSFP time-series data. (a) DW-SSFP time-series magnitude and phase data (blue) incorporating cardiac pulsatility + Gaussian noise (SNR = 20) synthesised using Monte Carlo simulations. Fitting to the data via the proposed EPG-Motion framework accurately characterises the DW-SSFP time-series profile (orange) in the measured data region (green box). (b) The estimated $V(t)$ time-series profile (reflecting the component of instantaneous velocity in the direction of the diffusion gradient across TRs) closely matches the ground truth in the measured data region (green), reflecting the possibility of characterising motion solely from the DW-SSFP signal. Dummy measurements (pink box) reflect a series of TRs where no comparison to the simulated data was performed. The white box reflects a series of TRs where the simulation reached a steady state. Here the dashed orange line represents the average estimate over the 10 noise repeats, with the orange shaded region surrounding the fitted line corresponding to the standard deviation over the 10 noise repeats.

Figure 6 displays the estimated diffusion coefficient from simulated pulsatile motion with varying SNR levels and maximum pulsatility velocity. Here we identify that the incorporation of motion properties in parameter estimation substantially reduces the misestimation of D. Specifically, no characterisation of subject motion (Figure 6a) led to biases in D of up to 275% across the investigated velocity/SNR regime, increasing as a function of the maximum pulsatile velocity. An equivalent investigation

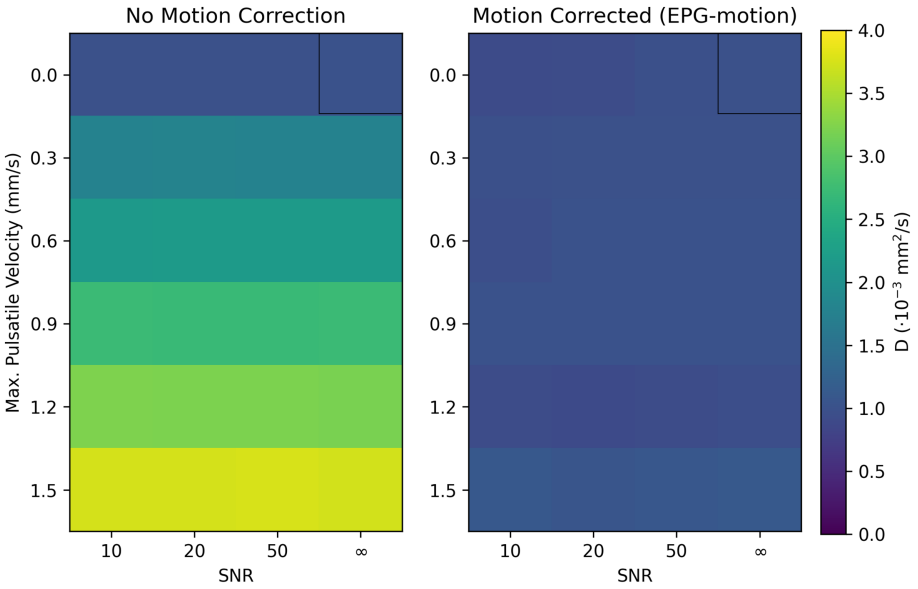

FIGURE 6 | Characterisation of D as a function of SNR and maximum pulsatile velocity amplitude. (a, b) The estimated diffusion coefficient, D, derived from DW-SSFP timeseries data as a function of SNR (x-axis) and maximum pulsatile velocity (y-axis). The two plots correspond to parameter estimation assuming (a) no motion correction and (b) motion correction using the proposed EPG-motion framework. The black box in the top right corresponds to the ground truth estimate (no motion, SNR = ∞). No incorporation of motion in parameter estimation (a) led to a maximum bias of 275% in the estimation of D across the investigated velocity/SNR regime, increasing as a function of the maximum pulsatile velocity. Simultaneous estimation of motion parameters (b) led to a maximum bias of 12%. Figure displays the average D calculated from 10 simulated DW-SSFP timeseries repeats per SNR/velocity level.

incorporating the estimation of motion parameters using the EPG-motion framework (Figure 6b) led to a maximum bias of 12%.

The motion-free simulations (Figure 6, top row) with no added noise (Figure 6, black box) estimated $0.998 \cdot 10^{-3}$ mm^2/s (with motion correction) and $1.000 \cdot 10^{-3}$ mm^2/s (no motion correction). A small bias was observed in the diffusion coefficient estimation at reduced SNR levels when incorporating motion correction (~8% at SNR = 10, Figure 6, top left) for the motion-free simulations, which were not present in the parameter estimation procedure without motion correction (~0.4% at SNR = 10). This reflects an increased sensitivity of the proposed EPG-motion framework to data noise.

Figure 7 displays an example DW-SSFP timeseries and $V(t)$ profile estimated in a single voxel of experimental data acquired in the human brain. The timeseries corresponds to the voxel in the thalamus, with the diffusion gradient oriented along the anterior–posterior axis. The experimental timeseries data display consistent characteristics to the DW-SSFP simulations incorporating cardiac pulsatility, with the periodicity of the DW-SSFP signal and $V(t)$ profile consistent with the recorded locations of pulse oximeter triggers.

Figure 8 displays the DW-SSFP timeseries magnitude data (b_{500}) across a portion of the cardiac cycle for Subject 1 with the diffusion gradient oriented along the (a) left–right, (b) anterior–posterior and (c) foot-head direction. Subtle changes in signal amplitude are visible across the timeseries in (a) and (b), with considerable changes in signal amplitude along the foot-head direction (c). Here, even a modest b-value of 500 s/mm^2 leads to a substantial loss of signal along the foot-head direction in central and anterior brain regions.

Equivalent figures are provided in Supporting Information for Subject 2 (Figure S5) and Subject 3 (Figure S6) for axial and coronal acquisitions. Coronal acquisitions display considerable motion-induced signal loss along the foot-head direction in central brain and brain stem regions. All three subjects offer similar orientation-dependent contrast, with Subject 2 displaying reduced signal levels in the anterior brain in comparison to Subject 1 and Subject 3 demonstrating a much greater loss of signal along the foot-head direction for both axial and coronal acquisitions, indicative of increased subject motion.

Figure 9 displays the corresponding $V(t)$ maps for Subject 1 estimated from the same portion of the cardiac cycle with the diffusion gradient oriented along the (a) left–right, (b) anterior–posterior and (c) foot-head direction. Here we observe smooth changes (both temporally and spatially) in $V(t)$. Importantly, each voxel in these images has been processed independently, with the arising spatial smoothness reflective of the consistency of velocity estimation across individual voxels. A notable exception arises from voxels in the centre of the brain along the foot-head direction (Figure 8c) where motion parameters could not be reliably estimated during peak systole (see Section 5).

The $V(t)$ maps display a consistent pattern of sharp velocity increases (associated with systole) followed by reduced velocities during diastole. The asymmetric $V(t)$ profile associated with the left–right gradient orientation is consistent with previous observations [52, 53] and an increased absolute velocity in the central

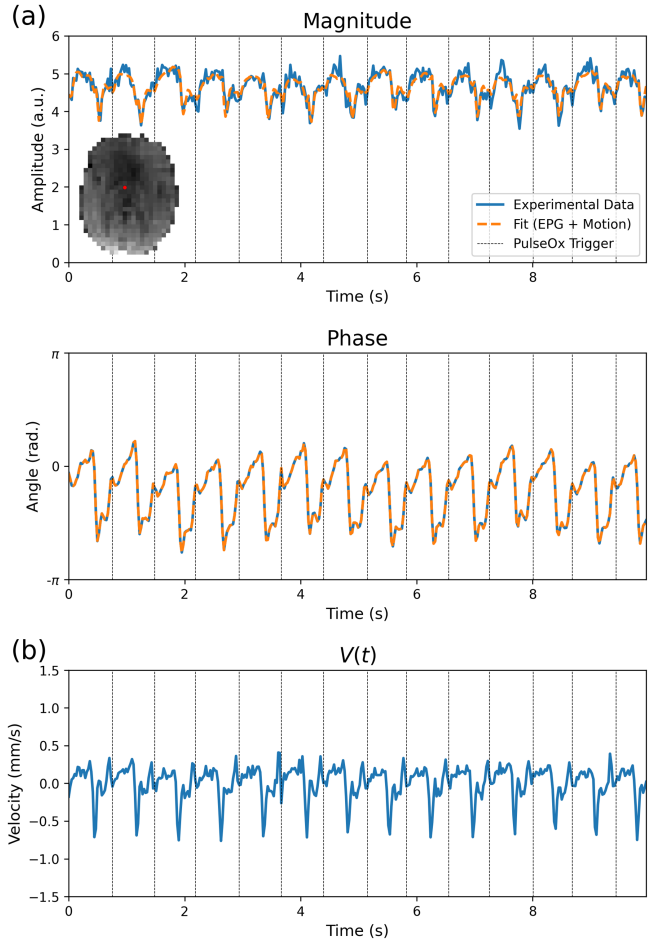

FIGURE 7 | DW-SSFP signal and $V(t)$ profile in a single voxel of experimental $b_{\text{eff}} = 500\ \text{s/mm}^2$ data. The experimental DW-SSFP signal profile (a) (blue lines) displays periodicity consistent with the timings of pulse oximeter triggers (black vertical lines) acquired as part of the acquisition. Fitting to the experimental data using the proposed EPG-motion framework (orange line) gives excellent agreement to the experimental data, with the estimated velocity profile (b) displaying consistent periodic changes in tissue velocity, consistent with pulse oximeter trigger locations. Displayed timeseries corresponds to a single voxel in the thalamus (visualised in inset figure of experimental data in (a)—red voxel) from Subject 1, with the diffusion gradient oriented along the anterior–posterior axis. $V(t)$ defined as the component of instantaneous velocity in the direction of the diffusion gradient across TRs (Equation 4).

brain along the anterior–posterior gradient orientation is consistent with Greitz et al. [44].

Figures S7 and S8 provide equivalent spatial $V(t)$ maps for Subjects 2 and 3. Coronal $V(t)$ profiles are consistent with the axial $V(t)$ profiles, with an asymmetric $V(t)$ profile for the left–right gradient orientation and increased absolute velocity in the central brain for the anterior–posterior gradient orientation. Subjects 2 and 3 provide smooth $V(t)$ maps for left–right and anterior–posterior gradient orientations, with noisier $V(t)$ estimates in comparison to Subject 1 along the foot-head orientation where parameters could not be reliably estimated. These findings are consistent with areas of reduced signal in the corresponding data (Figures S5 and S6).

Figure 10 displays tensor estimates reconstructed from the 12 diffusion gradient orientations in Subjects 1–3 (a–c) for DW-SSFP timeseries data without motion correction (top rows), DW-SSFP timeseries data with motion correction (middle rows) and DW-SE EPI data (bottom rows) for axial (left column) and coronal (right column) acquisitions. Without performing motion correction (a–c, top rows), it is not possible to reconstruct informative tensor estimates. Correction using the proposed EPG-motion framework leads to more consistent tensor estimates across the brain (a–c, middle rows). Motion corrected DW-SSFP data in Subjects 1 and 2 (a, b) give excellent visual agreement to DW-SE EPI data, with some small residual spatial biases in the centre of the brain for Subject 2 where motion is predicted to be greatest (Figure S7). Subject 3 displays considerable biases prior to motion correction (c, top row), with $L1$ estimates exceeding the presented data range ($5 \cdot 10^{-3}\ \text{mm}^2/\text{s}$). Following motion correction (c, middle row), diffusivity estimates are more in line with the DW-SE EPI estimates (c, bottom row). However, residual spatial biases remain in the data, most apparent in the $\vec{V}_1$ maps.

5 | Discussion

5.1 | EPG-Motion Framework

The proposed EPG-motion framework demonstrates that the impact of rigid body and pulsatile motion on the underlying magnetisation distribution of DW-SSFP leads to substantial changes in DW-SSFP signal magnitude and phase (Figures 3 and 4). Acquired experimental data incorporating a single-shot readout agrees visually with forward simulations arising from the EPG-motion framework, indicative of motion-induced signal corruption arising from magnetisation distribution of DW-SSFP (Figures 7–9). Without correction incorporating the proposed EPG-motion framework, diffusion coefficients are overestimated both theoretically (Figure 6a) and experimentally (Figure 10, top rows), with the degree of misestimation additionally dependent on the diffusion gradient orientation (Figure 10, top rows).

The proposed framework demonstrates that it is possible to model and correct for the impact of subject motion arising from the underlying magnetisation distribution retrospectively based on timeseries data capturing the evolution of the DW-SSFP signal, yielding parameter estimates with more consistent spatial contrast (Figure 10, middle rows) and agreement with complementary diffusion imaging methods (Figure 10, bottom rows). Motion-corrected data using the proposed EPG-motion framework attenuates the blue bias visible in earlier efforts to estimate tensors from motion-corrected DW-SSFP data [22], arising from the predominant motion-sensitivity of the DW-SSFP signal along the foot-head direction [22, 23].

The proposed motion operator introduced in Section 2 (building on a previous description [35]) is not specific to DW-SSFP and can be incorporated into EPG signal representations to investigate the impact of subject motion on arbitrary MRI sequences. Other methods that are anticipated to benefit from the concepts introduced in this manuscript include DW-DESS [39–41] and

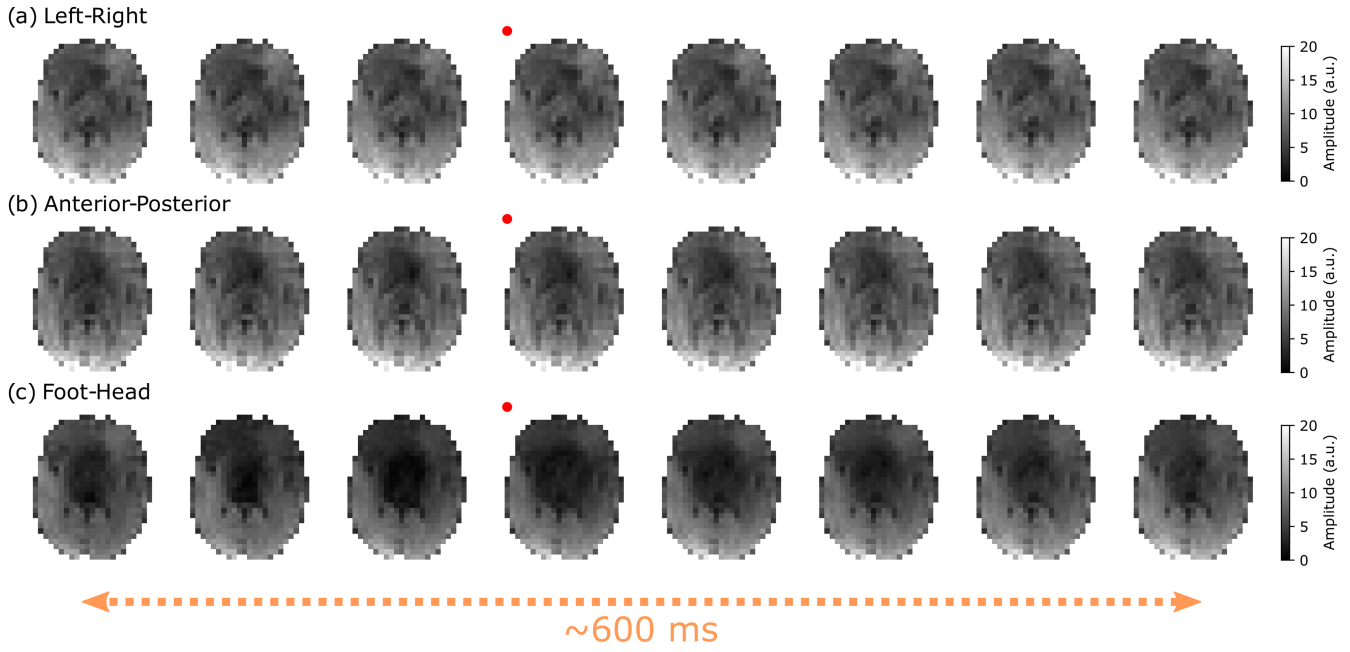

FIGURE 8 | Experimental DW-SSFP timeseries images (Subject 1). (a–c) Example b_{500} timeseries data acquired with left–right (a), anterior-posterior (b) and foot-head (c) gradient orientations in Subject 1. The change in signal is most prominent along the foot-head orientation, characterised by a substantial loss of signal in central and anterior brain regions. Here the red dots indicate the image acquired at the timepoint of the pulse oximeter trigger, with the x-axis reflecting a subset of data acquired over 624 ms, with a gap of 78 ms between images (three TRs). Corresponding figures for Subjects 2 and 3 are provided in Figures S5 and S6.

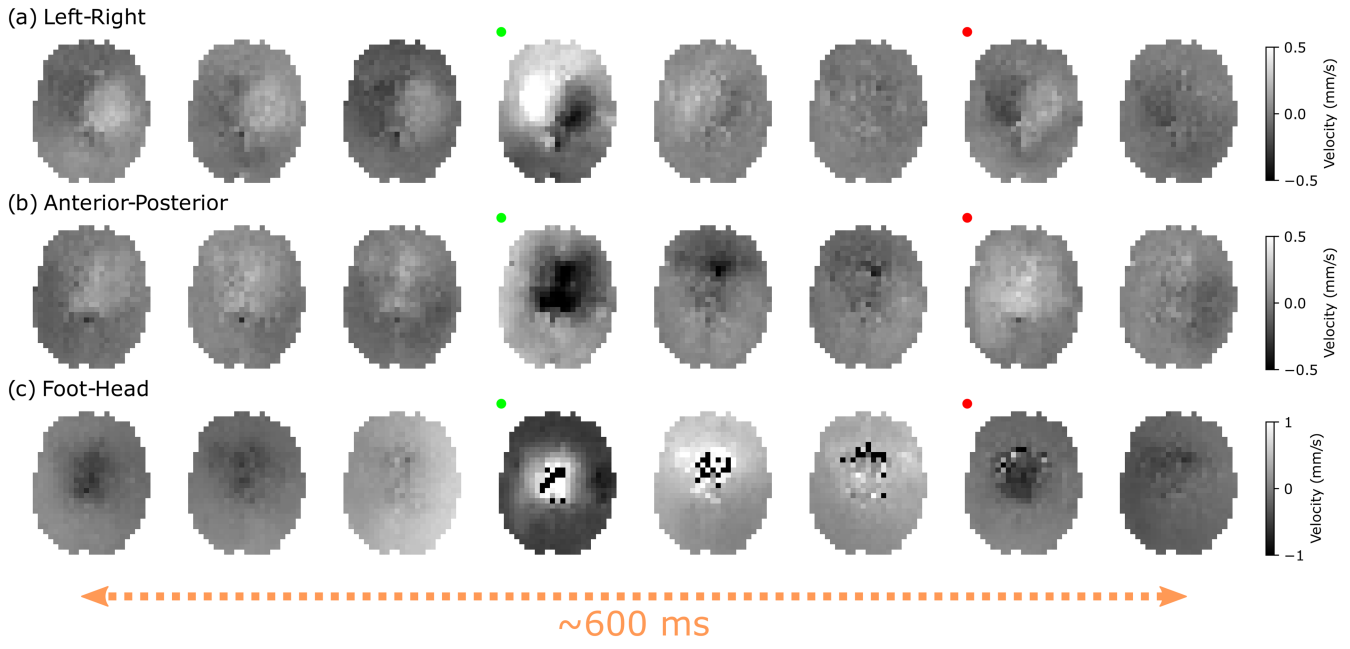

FIGURE 9 | Estimated $V(t)$ maps (Subject 1). (a–c) Example $V(t)$ spatial maps estimated from the experimental b_{500} DW-SSFP data acquired along left–right (a), anterior–posterior (b) and foot-head (c) gradient orientations in Subject 1. Here the red dots indicate the image acquired at the timepoint of the pulse oximeter trigger, with the green dots indicating peak brain tissue velocity changes. The x-axis reflects a subset of data acquired over 624 ms, with a gap of 78 ms between images (three TRs). $V(t)$ defined as the component of instantaneous velocity in the direction of the diffusion gradient across TRs (Equation 4). Black/white voxels within the brain correspond to velocities exceeding the colour bar limits (right-hand side). Corresponding figures for Subjects 2 and 3 are provided in Figures S7 and S8.

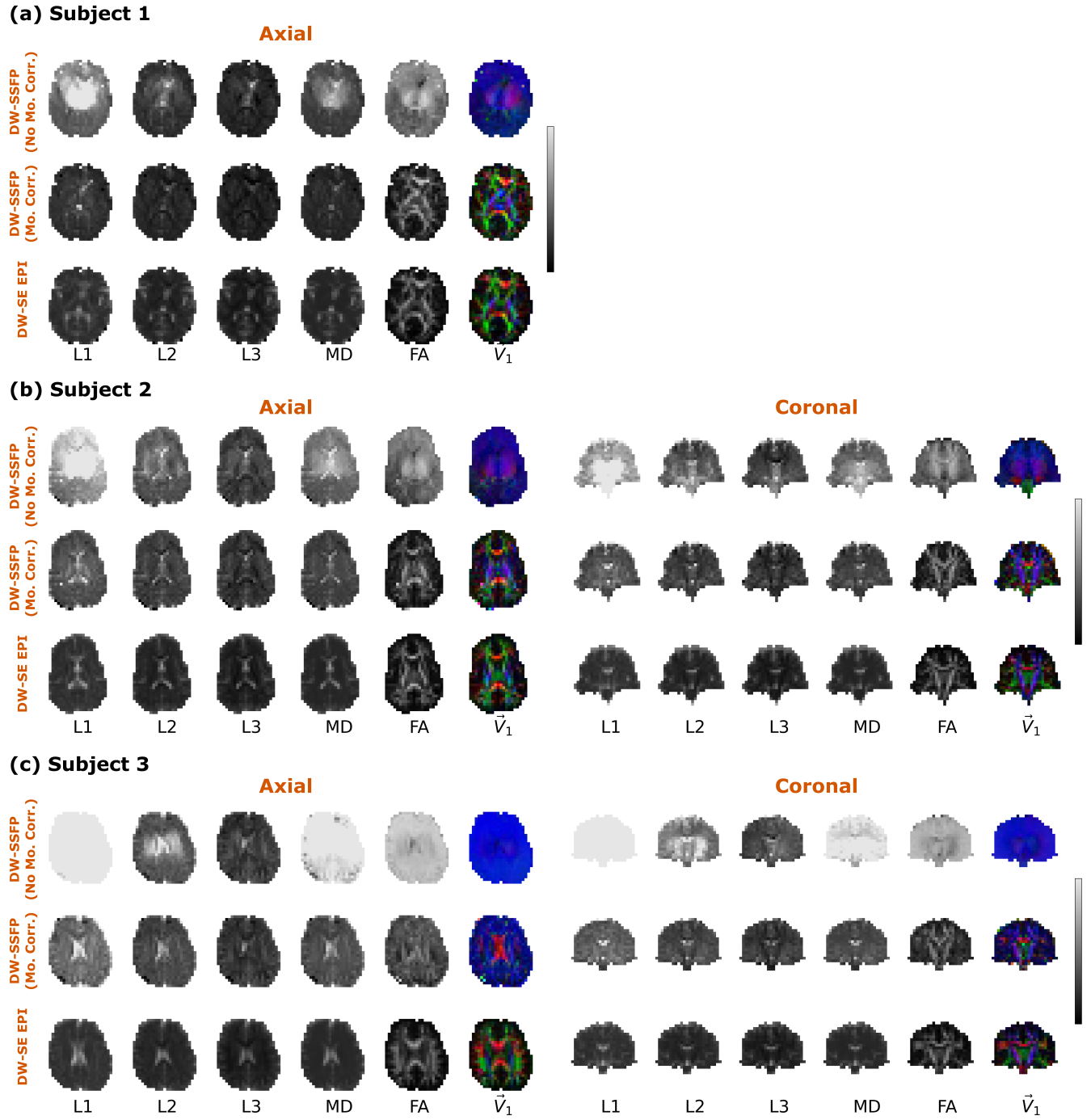

FIGURE 10 | Tensor outputs (all subjects). Comparison of tensor outputs for Subjects 1–3 (a–c) for DW-SSFP data without motion correction (top rows), DW-SSFP data with motion-correction (via the EPG-motion framework) (middle rows) and comparison DW-SE EPI data (bottom rows) for both axial (left column) and coronal (right column) acquisitions. Without motion-correction (a–c, top rows), DW-SSFP tensor estimates display large spatial biases. Motion-corrected DW-SSFP data (a–c, middle rows) display improved visual agreement with complementary DW-SE EPI estimates (a–c, bottom rows), attenuating spatial biases. Subjects 1 and 2 (a, b) offer similar motion correction performance. Subject 3 (c) displays poorer motion correction performance in comparison to Subjects 1 and 2, with greater residual spatial inhomogeneities remaining in the axial and coronal slices. Tensors reconstructed from individual diffusion coefficient maps estimated per orientation using custom code. To account for spurious diffusion coefficient estimates in the axial DW-SSFP data of Subject 3 (c, left column), the tensor reconstruction of the axial DW-SSFP data in Subject 3 only was inversely weighted by the variance the diffusion coefficient estimate (provided by SciPy *curve_fit*). Blue = foot-head, red = left–right, green = anterior–posterior. Greyscale colour bars reflect range between 0 and $5 \cdot 10^{-3}$ mm^2/s(L1/L2/L3/MD) and 0 to 1 (FA) (identical for all three subjects). L1 estimates without motion correction in Subjects 1 and 2 (centre of the brain) and L1/MD estimates in Subject 3 (whole slice) exceed the presented data range. Note that no coronal data were acquired in Subject 1, as described in Section 3.

MR fingerprinting [42, 43] methods, which are similarly sensitive to motion-induced signal loss arising from the weighted sum of magnetisation components with different evolution histories.

5.2 | Motion Characterisation During Systole

The estimated $V(t)$ maps (Figures 9 and S7 and S8) display smooth and consistent contrast across the brain during diastole and systole along left–right and anterior–posterior gradient orientations. $V(t)$ estimates along the foot-head gradient orientation (where subject motion is predicted to be largest) were noisier, with visualisation of the DW-SSFP data (Figures 8c, S5c and S6c) identifying that noisy motion parameter estimates are also associated with regions of low SNR. This suggests that parameter misestimation during systole is a likely consequence of (1) noise and/or (2) parameter degeneracies associated with rapid signal changes in high-velocity tissue regions.

To investigate this, Figures S9–S11 displays the spatial $V(t)$ maps estimated from the experimental b_{100} ($b_{\text{eff}} = 100\ \text{s/mm}^2$) data for Subjects 1–3. The spatial $V(t)$ maps display consistent contrast with the b_{500} ($b_{\text{eff}} = 500\ \text{s/mm}^2$) $V(t)$ maps (Figure 9), without noisy velocity estimates observed when the diffusion gradient is oriented along the foot-head axis. Figure S12 displays an example DW-SSFP timeseries and $V(t)$ profile from the b_{100} data set in a central brain (thalamus) voxel in Subject 1, demonstrating a periodic profile consistent with the pulse oximeter estimates.

The b_{500} data have intrinsically lower SNR and larger motion-induced signal changes versus the b_{100} data. Figure S13 displays the DW-SSFP timeseries and $V(t)$ profile for b_{500} data equivalent to Figure S12. Here we observe an excellent fit, with rapid magnitude/phase changes in the DW-SSFP signal and large non-physical oscillatory velocity estimates during systole exceeding 3 mm/s. Whilst the signal-forming mechanisms of DW-SSFP create a nontrivial relationship between sequence parameters and the maximum velocity that can be reliably estimated, the excellent fit combined with a consistent, oscillatory velocity profile during systole is indicative of degeneracies in the relationship between $V(t)$ and the measured signal.

For Subjects 1 and 2, misestimation of motion parameters during peak systole along the foot-head gradient orientation does not appear to significantly impact estimation of D both experimentally (Figure 10a,b) and in simulation (Figures 6 and S14). However, for Subject 3 spatial biases are still present following motion correction (Figure 10c). To investigate this further, Figure S15 displays the average timeseries velocity for all three subjects along the foot-head gradient orientation. Whilst Subjects 1 and 2 are characterised by more focal velocity changes in the brain centre and brainstem, Subject 3 was characterised by higher tissue velocities across the entire brain, most notably during the axial acquisition, indicative of rigid body motion. We anticipate that this led to a considerable perturbation of the DW-SSFP signal from steady-state, leading to substantial signal loss (Figure S6) that impact the performance of parameter estimation. Taken together, these findings motivate improved motion profile initialisation and regularisation to translate the findings presented here to a more generalisable motion-correction DW-SSFP scheme, as described below.

5.3 | Translation Into a Generalised DW-SSFP Acquisition and Reconstruction Framework

In this work, the proposed EPG-motion framework was applied to 2D, low-resolution single-shot DW-SSFP timeseries data. The acquired data are appropriate for validating the framework and understanding the origin of motion-induced artefacts arising from the signal-forming mechanisms of DW-SSFP, necessitating an EPG (or equivalent) framework to address, with the degree of motion corruption modulated by the local diffusion coefficient (Figures 4 and S4). The simplified fitting approach (non-linear least-squares, single motion estimate per TR, no regularisation) implemented independently for each voxel did not enforce any prior knowledge or constraints on the motion profile, with smooth spatial distributions of $V(t)$ (Figure 9) arising naturally from the parameter estimation procedure.

When considering a 3D, segmented readout DW-SSFP sequence, the impact of subject motion on reconstructed images will be more severe due to the additional contribution of phase/magnitude inconsistencies between individual k-space segments. To reduce the dimensionality of the reconstruction problem, the proposed framework could be integrated into a motion-reconstruction procedure that performs simultaneous parameter estimation across voxels considering a smoothly varying spatial and temporal motion profile. Pulsatile velocity estimation could initialised with information from complementary methods (e.g., phase contrast imaging [54], DENSE [52, 55], Amplified MRI [53, 56]) and combined with ECG/Pulse oximeter measurements acquired during DW-SSFP acquisition to regularise the fitting procedure. This information could be leveraged with sequences integrating navigators and non-cartesian readouts to establish motion-robust DW-SSFP acquisition schemes.

6 | Conclusion

We demonstrate that it is possible to model and correct for the impact of subject motion on the magnetisation distribution of DW-SSFP, with motion-corrected experimental DW-SSFP data displaying reduced spatial biases and more consistent contrast with DW-SE EPI tensor estimates. The proposed framework is entirely open source, facilitating future investigations into the impact of motion on DW-SSFP acquisitions.

Acknowledgments

B.C.T. is funded by a Sir Henry Wellcome Postdoctoral Fellowship (Wellcome Trust) (222829/Z/21/Z). W.W. is funded by the Royal Academy of Engineering (RF\201819\18\92). K.L.M. is funded by a Wellcome Trust Senior Research Fellowship (224573/Z/21/Z). This research was supported by the NIHR Oxford Health Biomedical Research Centre (NIHR203316). The views expressed are those of the author(s) and not necessarily those of the NIHR or the Department of Health and Social Care. The Centre for Integrative Neuroimaging was supported by core funding from the Wellcome Trust (203139/Z/16/Z and 203139/A/16/Z). This research was funded in whole, or in part, by the Wellcome Trust (222829/Z/21/Z, 224573/Z/21/Z, 203139/Z/16/Z, 203139/A/16/Z). For the purpose of open access, the author has applied a CC BY public copyright license to any Author Accepted Manuscript version arising from this submission.

Funding

This work was supported by the Royal Academy of Engineering (RF\201819\18\92), the NIHR Oxford Health Biomedical Research Centre (NIHR203316), the Wellcome Trust (222829/Z/21/Z, 224573/Z/21/Z, 203139/Z/16/Z, 203139/A/16/Z).

Data Availability Statement

The released software (available at github.com/BenjaminTendler/MotionCorrectionDWSSFP, SHA #d0ca7b637a87f96b8c60e3356ce7f9ad85eefc53) provides a framework to investigate the impact of motion on the DW-SSFP signal, allowing for the forward simulation of temporal motion profiles for 1D, 2D and 3D imaging volumes, the resulting DW-SSFP signal and estimation of motion parameters from DW-SSFP timeseries data. Scripts to replicate many of the figures presented in this manuscript are also provided.

References

1. E. O. Stejskal and J. E. Tanner, "Spin Diffusion Measurements: Spin Echoes in the Presence of a Time-Dependent Field Gradient," *Journal of Chemical Physics* 42 (1965): 288–292, https://doi.org/10.1063/1.1695690.

2. T. L. Chenevert and J. G. Pipe, "Effect of Bulk Tissue Motion on Quantitative Perfusion and Diffusion Magnetic Resonance Imaging," *Magnetic Resonance in Medicine* 19, no. 2 (1991): 261–265.

3. A. W. Anderson and J. C. Gore, "Analysis and Correction of Motion Artifacts in Diffusion Weighted Imaging," *Magnetic Resonance in Medicine* 32, no. 3 (1994): 379–387.

4. T. L. Chenevert, J. G. Pipe, D. M. Williams, and J. A. Brunberg, "Quantitative Measurement of Tissue Perfusion and Diffusion In Vivo," *Magnetic Resonance in Medicine* 17, no. 1 (1991): 197–212.

5. R. Turner and D. Le Bihan, "Single-Shot Diffusion Imaging at 2.0 Tesla," *Journal of Magnetic Resonance* 86, no. 3 (1990): 445–452.

6. R. Turner, D. Le Bihan, J. Maier, R. Vavrek, L. K. Hedges, and J. Pekar, "Echo-Planar Imaging of Intravoxel Incoherent Motion," *Radiology* 177, no. 2 (1990): 407–414.

7. V. J. Wedeen, R. M. Weisskoff, and B. P. Poncelet, "MRI Signal Void due to In-Plane Motion Is All-Or-None," *Magnetic Resonance in Medicine* 32, no. 1 (1994): 116–120.

8. P. Storey, F. J. Frigo, R. S. Hinks, et al., "Partial k-Space Reconstruction in Single-Shot Diffusion-Weighted Echo-Planar Imaging," *Magnetic Resonance in Medicine* 57, no. 3 (2007): 614–619.

9. J. L. R. Andersson, M. S. Graham, E. Zsoldos, and S. N. Sotiropoulos, "Incorporating Outlier Detection and Replacement Into a Non-Parametric Framework for Movement and Distortion Correction of Diffusion MR Images," *NeuroImage* 141 (2016): 556–572.

10. D. Le Bihan, "Intravoxel Incoherent Motion Imaging Using Steady-State Free Precession," *Magnetic Resonance in Medicine* 7 (1988): 346–351, https://doi.org/10.1002/mrm.1910070312.

11. K. D. Merboldt, W. Hänicke, M. L. Gyngell, J. Frahm, and H. Bruhn, "Rapid NMR Imaging of Molecular Self-Diffusion Using a Modified CE-FAST Sequence," *Journal of Magnetic Resonance* 82 (1989): 115–121, https://doi.org/10.1016/0022-2364(89)90170-4.

12. K. Merboldt, H. Bruhn, J. Frahm, M. L. Gyngell, W. Hänicke, and M. Deimling, "MRI of 'Diffusion' in the Human Brain: New Results Using a Modified CE-FAST Sequence," *Magnetic Resonance in Medicine* 9 (1989): 423–429, https://doi.org/10.1002/mrm.1910090316.

13. R. Kaiser, E. Bartholdi, and R. R. Ernst, "Diffusion and Field-Gradient Effects in NMR Fourier Spectroscopy," *Journal of Chemical Physics* 60 (1974): 2966–2979, https://doi.org/10.1063/1.1681477.

14. R. B. Buxton, "The Diffusion Sensitivity of Fast Steady-State Free Precession Imaging," *Magnetic Resonance in Medicine* 29 (1993): 235–243, https://doi.org/10.1002/mrm.1910290212.

15. B. C. Tendler, "Investigating Time-Independent and Time-Dependent Diffusion Phenomena Using Steady-State Diffusion MRI," *Scientific Reports* 15, no. 1 (2025): 3580.

16. J. A. McNab, S. Jbabdi, S. C. L. Deoni, G. Douaud, T. E. J. Behrens, and K. L. Miller, "High Resolution Diffusion-Weighted Imaging in Fixed Human Brain Using Diffusion-Weighted Steady State Free Precession," *NeuroImage* 46 (2009): 775–785, https://doi.org/10.1016/j.neuroimage.2009.01.008.

17. K. L. Miller, B. A. Hargreaves, G. E. Gold, and J. M. Pauly, "Steady-State Diffusion-Weighted Imaging of In Vivo Knee Cartilage," *Magnetic Resonance in Medicine* 51 (2004): 394–398, https://doi.org/10.1002/mrm.10696.

18. E. Bosak and P. R. Harvey, "Navigator Motion Correction of Diffusion Weighted 3D SSFP Imaging," *Magnetic Resonance Materials in Physics, Biology and Medicine* 12 (2001): 167–176.

19. K. L. Miller and J. M. Pauly, "Nonlinear Phase Correction for Navigated Diffusion Imaging," *Magnetic Resonance in Medicine* 50, no. 2 (2003): 343–353.

20. Y. Jung, A. A. Samsonov, W. F. Block, et al., "3D Diffusion Tensor MRI With Isotropic Resolution Using a Steady-State Radial Acquisition," *Journal of Magnetic Resonance Imaging* 29, no. 5 (2009): 1175–1184.

21. J. A. McNab, D. Gallichan, and K. L. Miller, "3D Steady-State Diffusion-Weighted Imaging With Trajectory Using Radially Batched Internal Navigator Echoes (TURBINE)," *Magnetic Resonance in Medicine* 63, no. 1 (2010): 235–242.

22. R. L. O'Halloran, M. Aksoy, A. T. Van, and R. Bammer, "3D Isotropic High-Resolution Diffusion-Weighted MRI of the Whole Brain With a Motion-Corrected Steady-State Free Precession Sequence," *Magnetic Resonance in Medicine* 70, no. 2 (2013): 466–478.

23. R. O'Halloran, M. Aksoy, E. Aboussouan, E. Peterson, A. Van, and R. Bammer, "Real-Time Correction of Rigid Body Motion-Induced Phase Errors for Diffusion-Weighted Steady-State Free Precession Imaging," *Magnetic Resonance in Medicine* 73, no. 2 (2015): 565–576.

24. O. Bieri, C. Ganter, G. H. Welsch, S. Trattnig, T. C. Mamisch, and K. Scheffler, "Fast Diffusion-Weighted Steady State Free Precession Imaging of In Vivo Knee Cartilage," *Magnetic Resonance in Medicine* 67 (2012): 691–700, https://doi.org/10.1002/mrm.23061.

25. Z. W. Zhang, L. J. Song, Q. F. Meng, et al., "High-Resolution Diffusion-Weighted MR Imaging of the Human Lumbosacral Plexus and Its Branches Based on a Steady-State Free Precession Imaging Technique at 3T," *American Journal of Neuroradiology* 29, no. 6 (2008): 1092–1094.

26. R. L. Ehman and J. P. Felmlee, "Adaptive Technique for High-Definition MR Imaging of Moving Structures," *Radiology* 173, no. 1 (1989): 255–263.

27. K. Butts, A. de Crespigny, J. M. Pauly, and M. Moseley, "Diffusion-Weighted Interleaved Echo-Planar Imaging With a Pair of Orthogonal Navigator Echoes," *Magnetic Resonance in Medicine* 35, no. 5 (1996): 763–770.

28. J. G. Pipe, "Motion Correction With PROPELLER MRI: Application to Head Motion and Free-Breathing Cardiac Imaging," *Magnetic Resonance in Medicine* 42, no. 5 (1999): 963–969.

29. J. G. Pipe, "Multishot Diffusion Weighted FSE With PROPELLER," in *Proceedings of the 9th Annual Scientific Meeting of ISMRM, Glasgow* (2001).

30. D. h. Kim, E. Adalsteinsson, and D. M. Spielman, "Simple Analytic Variable Density Spiral Design," *Magnetic Resonance in Medicine* 50, no. 1 (2003): 214–219.

31. C. Liu, R. Bammer, D. h. Kim, and M. E. Moseley, "Self-Navigated Interleaved Spiral (SNAILS): Application to High-Resolution Diffusion Tensor Imaging," *Magnetic Resonance in Medicine* 52, no. 6 (2004): 1388–1396.

32. N. k. Chen, A. Guidon, H. C. Chang, and A. W. Song, "A Robust Multi-Shot Scan Strategy for High-Resolution Diffusion Weighted MRI Enabled by Multiplexed Sensitivity-Encoding (MUSE)," *NeuroImage* 72 (2013): 41–47.

33. M. Mani, M. Jacob, D. Kelley, and V. Magnotta, "Multi-Shot Sensitivity-Encoded Diffusion Data Recovery Using Structured Low-Rank Matrix Completion (MUSSELS)," *Magnetic Resonance in Medicine* 78, no. 2 (2017): 494–507.

34. J. P. Wansapura, S. K. Holland, R. S. Dunn, and J. W. S. Ball, "NMR Relaxation Times in the Human Brain at 3.0 Tesla," *Journal of Magnetic Resonance Imaging* 9, no. 4 (1999): 531–538.

35. M. Weigel, "Extended Phase Graphs: Dephasing, RF Pulses, and Echoes – Pure and Simple," *Journal of Magnetic Resonance Imaging* 41 (2015): 266–295, https://doi.org/10.1002/jmri.24619.

36. B. C. Tendler, "Theoretical Framework to Characterise Motion Artefacts Arising From Steady-State Diffusion MRI," in *European Society of Magnetic Resonance in Medicine & Biology (ESMRMB) Annual Scientific Meeting* (2023), LB298.

37. F. Bloch, "Nuclear Induction," *Physics Review* 70, no. 7–8 (1946): 460–474, https://doi.org/10.1103/PhysRev.70.460.

38. M. Weigel, S. Schwenk, V. G. Kiselev, K. Scheffler, and J. Hennig, "Extended Phase Graphs With Anisotropic Diffusion," *Journal of Magnetic Resonance* 205, no. 2 (2010): 276–285.

39. C. J. Moran, J. Y. Cheng, C. M. Sandino, et al., "Diffusion-Weighted Double-Echo Steady-State With a Three-Dimensional Cones Trajectory for Non-Contrast-Enhanced Breast MRI," *Journal of Magnetic Resonance Imaging* 53, no. 5 (2021): 1594–1605.

40. O. Bieri, C. Ganter, and K. Scheffler, "Quantitative In Vivo Diffusion Imaging of Cartilage Using Double Echo Steady-State Free Precession," *Magnetic Resonance in Medicine* 68, no. 3 (2012): 720–729.

41. E. Staroswiecki, K. L. Granlund, M. T. Alley, G. E. Gold, and B. A. Hargreaves, "Simultaneous Estimation of T2 and Apparent Diffusion Coefficient in Human Articular Cartilage In Vivo With a Modified Three-Dimensional Double Echo Steady State (DESS) Sequence at 3 T," *Magnetic Resonance in Medicine* 67, no. 4 (2012): 1086–1096.

42. Y. Wang, Y. Lin, D. Cui, E. S. K. Hui, E. Y. P. Lee, and P. Cao, "Distortion-Free Steady-State Diffusion-Weighted Imaging With Magnetic Resonance Fingerprinting," *Medical Physics* 52 (2025).

43. M. Afzali, L. Mueller, K. Sakaie, et al., "MR Fingerprinting With b-Tensor Encoding for Simultaneous Quantification of Relaxation and Diffusion in a Single Scan," *Magnetic Resonance in Medicine* 88, no. 5 (2022): 2043–2057.

44. D. Greitz, R. Wirestam, A. Franck, B. Nordell, C. Thomsen, and F. Ståhlberg, "Pulsatile Brain Movement and Associated Hydrodynamics Studied by Magnetic Resonance Phase Imaging: The Monro-Kellie Doctrine Revisited," *Neuroradiology* 34 (1992): 370–380.

45. M. Jenkinson, C. F. Beckmann, T. E. J. Behrens, M. W. Woolrich, and S. M. Smith, "FSL - Review," *NeuroImage* 62 (2012): 782–790, https://doi.org/10.1016/j.neuroimage.2011.09.015.

46. M. G. Hall and D. C. Alexander, "Convergence and Parameter Choice for Monte-Carlo Simulations of Diffusion MRI," *IEEE Transactions on Medical Imaging* 28 (2009): 1354–1364, https://doi.org/10.1109/TMI.2009.2015756.

47. K. L. Miller, J. A. McNab, S. Jbabdi, and G. Douaud, "Diffusion Tractography of Post-Mortem Human Brains: Optimization and Comparison of Spin Echo and Steady-State Free Precession Techniques," *NeuroImage* 59 (2012): 2284–2297, https://doi.org/10.1016/j.neuroimage.2011.09.054.

48. P. Ehses, "Open Source Software: MapVBVD," 2022, github.com/pehses/mapVBVD.

49. B. Bilgic, J. R. Polimeni, L. L. Wald, and K. Setsompop, "Automated Tissue Phase and QSM Estimation From Multichannel Data," in *Proceedings of the 24th Annual Meeting of ISMRM, Singapore* (2016), 2849.

50. B. Bilgic, "Open Source Software: SVD for Reference-Free Coil Combination at High Field," 2022, martinos.org/~berkin/software.html.

51. P. Ehses, D. Brenner, R. Stirnberg, E. D. Pracht, and T. Stöcker, "Whole-Brain B1-Mapping Using Three-Dimensional DREAM," *Magnetic Resonance in Medicine* 82, no. 3 (2019): 924–934.

52. A. L. Adams, H. J. Kuijf, M. A. Viergever, P. R. Luijten, and J. J. M. Zwanenburg, "Quantifying Cardiac-Induced Brain Tissue Expansion Using DENSE," *NMR in Biomedicine* 32, no. 2 (2019): e4050.

53. I. Terem, K. Younes, N. Wang, et al., "3D Quantitative-Amplified Magnetic Resonance Imaging (3D q-aMRI)," *Bioengineering* 11, no. 8 (2024): 851.

54. N. J. Pelc, R. J. Herfkens, A. Shimakawa, and D. R. Enzmann, "Phase Contrast Cine Magnetic Resonance Imaging," *Magnetic Resonance Quarterly* 7, no. 4 (1991): 229–254.

55. X. Zhong, C. H. Meyer, D. J. Schlesinger, et al., "Tracking Brain Motion During the Cardiac Cycle Using Spiral Cine-DENSE MRI," *Medical Physics* 36, no. 8 (2009): 3413–3419.

56. S. J. Holdsworth, M. S. Rahimi, W. W. Ni, G. Zaharchuk, and M. E. Moseley, "Amplified Magnetic Resonance Imaging (aMRI)," *Magnetic Resonance in Medicine* 75, no. 6 (2016): 2245–2254.

Supporting Information

Additional supporting information can be found online in the Supporting Information section. **Figure S1:** Pulsatility time-series velocity profile. Relative velocity timeseries profile was based visually on the experimental thalamus (caudal) profile presented in Greitz et al. Profile defined modelling systole as a function of $A \cdot \sin \frac{4\pi \cdot \mathrm{HR} \cdot t}{60}$ over 1/4 of the cardiac cycle, where A = maximum pulsatile velocity (mm/s), HR = heart rate (beats/min) and t = time. Displacement (i.e., integral of the velocity profile) across a single cardiac cycle was set equal to zero, with the velocity profile defined as constant during diastole. Above profile synthesised setting HR = 50 beats/min. **Figure S2:** Pulsatility spatial velocity map. Relative spatial velocity profile was based visually on the experimental caudal velocity maps presented in Greitz et al. Here, the velocity map displays the relative maximum spatial velocity associated with brain pulsatility, and is used to rescale the cardiac pulsatility time-series profile (Figure S1) in each voxel. Profile defined as a function of $\frac{(-r+c)^3}{c^3}$, where r = relative voxel position (mm), and c = constant (mm). Here $c = 175$ mm, preserving the spatial velocity profile for datasets with different voxel sizes or fields of view. **Figure S3:** Impact of motion on DW-SE images. Here we display simulated single-shot DW-SE images with an instantaneous readout, incorporating (a) no motion (b) constant translation along the foot-head direction ($\vec{v} = [0, 0, 0.2]$ mm/s), (c) constant rotation with the axis of rotation oriented along the left–right direction (i.e., passing through the sagittal plane) ($\vec{\omega} = [0.2, 0, 0]^{\circ}$/s), and (d) cardiac pulsatility along the foot-head direction ($\vec{v}_{\mathrm{Card}} = [0, 0, 0.4]$ mm/s), simulated with the diffusion gradient oriented along the foot-head direction ($\hat{g} = [0, 0, 1]$). Images synthesised using the HCP1065 DTI template Mean Diffusivity map, available as part of FSL. Cardiac pulsatility timeseries profile and relative velocity map provided in Figures S1 and S2. Sequence parameters based on the experimental investigation performed in Miller and Pauly (defining the TR in DW-SSFP as the DW-SE diffusion time), setting $G = 40$ mT/m, $\delta = 6.5$ ms, $\alpha = 30^{\circ}$, $\Delta = 40$ ms, $\phi = 0^{\circ}$. Relaxation parameters (set equal across all voxels) were based on approximate in vivo values in brain tissue at $3T$, setting $T_1 = 832$ ms and $T_2 = 110$ ms.

Voxels were modelled as independent (i.e., the voxel location is stationary over the time-course of the simulation). **Figure S4:** Interplay between the diffusion coefficient and motion-induced signal changes. Relative to motion-free simulations, (a) and (b) display the signal amplitude and phase change arising from subject motion as a function of D. Higher D leads to a reduced change in signal amplitude and phase, analogous to reduced motion sensitivity. To understand this further, (c) displays the relative diffusion attenuation (log scale) as a function of pathway dephasing order (k). Here, increased D (orange line) is associated with a faster loss of the relative signal as a function of k. The relative phase difference arising from motion scales linearly as a function of k_j, and is independent of D (d). Taken together, tissues with increased D have reduced motion sensitivity arising from the reduced contribution of pathways with high k. Motion simulated as a constant translation along a single dimension ($\vec{v} = [0, 0, 0.2]$ mm/s). Sequence parameters based on the experimental investigation performed in Miller and Pauly, setting $G = 40$ mT/m, $\delta = 6.5$ ms, $\alpha = 30^{o}$, TR = 40 ms, $\phi = 0^{o}$ and $\hat{g} = [0, 0, 1]$. Relaxation parameters (set equal across all voxels) were based on approximate in vivo values in brain tissue at 3T, setting $T_1 = 832$ ms and $T_2 = 110$ ms. **Figure S5:** Experimental DW-SSFP timeseries images (Subject 2). Equivalent to Figure 8 in the main text, (a–c) correspond to example b_{500} timeseries data acquired with left–right (a), anterior-posterior (b) and foot-head (c) gradient orientations for an axial (top) and coronal (bottom) slice in Subject 2. The change in signal is most prominent along the foot-head orientation, characterised here by a substantial loss of signal in several brain regions. Red dots indicate the image acquired at the timepoint of the pulse oximeter trigger, with the x-axis reflecting a subset of data acquired over 832 ms, with a gap of 104 ms between images (four TRs). Anterior–posterior images shifted temporally by 54 ms (two TRs) relative to left–right and foot-head orientations. Images have an identical dynamic range to Figure 8 (in the main text). **Figure S6:** Experimental DW-SSFP timeseries images (Subject 3). Equivalent to Figure 8 in the main text, (a–c) correspond to example b_{500} timeseries data acquired with left–right (a), anterior-posterior (b) and foot-head (c) gradient orientations for an axial (top) and coronal (bottom) slice in Subject 3. The change in signal is most prominent along the foot-head orientation, with an increased level of signal loss in comparison to Subject 1 (Figure 8) and Subject 2 (Figure S5), indicative of increased subject motion. Red dots indicate the image acquired at the timepoint of the pulse oximeter trigger, with the x-axis reflecting a subset of data acquired over 832 ms, with a gap of 104 ms between images (four TRs). Images have an identical dynamic range to Figure 8 (in the main text) and Figure S5. **Figure S7:** Estimated $V(t)$ maps (Subject 2). Equivalent to Figure 9 in the main text, (a–c) correspond to example $V(t)$ spatial maps estimated from the experimental b_{500} DW-SSFP data along left–right (a), anterior–posterior (b), and foot-head (c) gradient orientations for an axial (top) and coronal (bottom) slice in Subject 2. Here the red dots indicate the image acquired at the timepoint of the pulse oximeter trigger, with the green dots indicating peak brain tissue velocity changes. The x-axis reflects a subset of data acquired over 832 ms, with a gap of 104 ms between images (four TRs). Anterior–posterior images shifted temporally by 54 ms (two TRs) relative to left–right and foot-head orientations. $V(t)$ defined as the component of instantaneous velocity in the direction of the diffusion gradient across TRs (Equation 4). Black/white voxels within the brain correspond to velocities exceeding the colour bar limits (right-hand side). Velocity maps have an increased dynamic range in comparison to Figure 9 (in the main text). **Figure S8:** Estimated $V(t)$ maps (Subject 3). Equivalent to Figure 9 in the main text, (a–c) correspond to example $V(t)$ spatial maps estimated from the experimental b_{500} DW-SSFP data along left–right (a), anterior–posterior (b) and foot-head (c) gradient orientations for an axial (top) and coronal (bottom) slice in Subject 3. Here the red dots indicate the image acquired at the timepoint of the pulse oximeter trigger, with the green dots indicating peak brain tissue velocity changes. The x-axis reflects a subset of data acquired over 832 ms, with a gap of 104 ms between images (four TRs). $V(t)$ defined as the component of instantaneous velocity in the direction of the diffusion gradient across TRs (Equation 4). Black/white voxels within the brain correspond to velocities exceeding the colour bar limits (right-hand side). Velocity maps have an increased dynamic range in comparison to Figure 9 (in the main text) (all gradient orientations) and Figure S7 (left–right and anterior–posterior gradient orientations). **Figure S9:** Estimated b_{100} $V(t)$ maps (Subject 1). (a–c) $V(t)$ maps estimated from the experimental DW-SSFP $b_{\text{eff}} = 100$ s/mm^2 data along the left–right (a), anterior-posterior (b), and foot-head (c) gradient orientations over the cardiac cycle. The displayed maps are equivalent to the b_{500} maps displayed in Figure 9 (in the main text), where $V(t)$ maps are more consistently estimated along the foot-head direction. Here the red dots indicate the image acquired at the timepoint of the pulse oximeter trigger, with the green dots indicating peak brain tissue velocity changes. The x-axis reflects a subset of data acquired over 624 ms, with a gap of 78 ms between images (three TRs). $V(t)$ defined as the component of instantaneous velocity in the direction of the diffusion gradient across TRs (Equation 4). Black/white voxels within the brain correspond to velocities less/greater than the colour bar limits (right-hand side). Corresponding figures for Subjects 2 and 3 are provided in Figures S10 and S11. **Figure S10:** Estimated b_{100} $V(t)$ maps (Subject 2). Equivalent to Figure S9, here we display $V(t)$ maps estimated from the experimental DW-SSFP $b_{\text{eff}} = 100$ s/mm^2 data along the left–right (a), anterior-posterior (b), and foot-head (c) gradient orientations over the cardiac cycle for an axial (top) and coronal (bottom) slice in Subject 2. The displayed maps are equivalent to the b_{500} maps displayed in Figure S7, where $V(t)$ maps are more consistently estimated along the foot-head direction. Here the red dots indicate the image acquired at the timepoint of the pulse oximeter trigger, with the green dots indicating peak brain tissue velocity changes. The x-axis reflects a subset of data acquired over 832 ms, with a gap of 104 ms between images (four TRs). $V(t)$ defined as the component of instantaneous velocity in the direction of the diffusion gradient across TRs (Equation 4). Black/white voxels within the brain correspond to velocities less/greater than the colour bar limits (right-hand side). Velocity maps have an increased dynamic range in comparison to Figure S9. **Figure S11:** Estimated b_{100} $V(t)$ maps (Subject 3). Equivalent to Figures S9 and S10, here we display V (t) maps estimated from the experimental DW-SSFP $b_{\text{eff}} = 100$ s/mm^2 data along the left–right (a), anterior-posterior (b), and foot-head (c) gradient orientations over the cardiac cycle for an axial (top) and coronal (bottom) slice in Subject 2. The displayed maps are equivalent to the b_{500} maps displayed in Figure S8, where V (t) maps are more consistently estimated along the foot-head direction. Here the red dots indicate the image acquired at the timepoint of the pulse oximeter trigger, with the green dots indicating peak brain tissue velocity changes. The x-axis reflects a subset of data acquired over 832 ms, with a gap of 104 ms between images (four TRs). $V(t)$ defined as the component of instantaneous velocity in the direction of the diffusion gradient across TRs (Equation 4). Black/white voxels within the brain correspond to velocities less/greater than the colour bar limits (right-hand side). Velocity maps have an increased dynamic range in comparison to Figure S9 (all gradient orientations) and Figure S10 (left–right and anterior–posterior gradient orientations). **Figure S12:** DW-SSFP signal and $V(t)$ profile in a single voxel of experimental b_{100} data. Identical in structure to Figure 7 (in the main text), here we display an experimental (blue lines) and estimated (orange lines) DW-SSFP signal profile (a) and the $V(t)$ profile (b) for a single voxel of $b_{\text{eff}} = 100$ s/mm^2 data acquired in the thalamus (visualised

in inset figure of experimental data in (a)—red voxel), with the diffusion gradient oriented along the foot-head axis. Black vertical lines correspond to pulse oximeter trigger timings acquired as part of the acquisition. $V(t)$ does not exceed 1.5 mm/s (maximum 1.26 mm/s), with the change in velocity per TR below 1 mm/s (maximum 0.86 mm/s/TR). DW-SSFP signal multiplied by e^{-i} to facilitate visualisation of wrapped phase data. **Figure S13:** DW-SSFP signal and $V(t)$ profile in a single voxel of experimental $b_{\text{eff}} = 500$ s/mm^2 data. Identical in structure to Figure S12, here we display an experimental (blue lines) and estimated (orange lines) DW-SSFP signal profile (a) and the $V(t)$ profile (b) for a single voxel of b_{500} data acquired in the thalamus (visualised in inset figure of experimental data in (a)—red voxel), with the diffusion gradient oriented along the foot-head axis. Black vertical lines correspond to pulse oximeter trigger timings acquired as part of the acquisition. $V(t)$ estimates a consistent rapidly oscillating velocity profile during systole with velocity values routinely exceeding 3 mm/s, far greater than the equivalent velocity profile estimated from the b_{100} data (Figure S12). DW-SSFP signal multiplied by e^{-i} to facilitate visualisation of wrapped phase data. **Figure S14:** Simulated and estimated $V(t)$ profiles. Here we display the simulated (blue) and estimated (orange) $V(t)$profiles (V_{max} ranging from 0 to 1.5 mm/s) from noiseless data, with sequence parameters based on the experimental investigation performed in Miller and Pauly, setting $G = 40$ mT/m, $\delta = 6.5$ ms, $\alpha = 30^{\text{o}}$, TR = 40 ms and $\phi = 0^{\text{o}}$. Excellent agreement is given over the $V(t)$profiles for velocities below 1 mm/s, with errors in velocity estimation during systole at 1.2 and 1.5 mm/s. Despite the discrepancy during systole, the diffusion coefficient can still be reliably estimated (Figure 6). Velocity estimation during systole could be improved with more robust initialisation of the velocity profile based on expected pulsatility waveforms or complementary data (see Discussion). $V(t)$ defined as the component of instantaneous velocity in the direction of the diffusion gradient across TRs (Equation 4). **Figure S15:** Average absolute velocity along the foot-head gradient orientation. Here we display $V(t)$ maps representing the average absolute velocity of the timeseries data for all three subjects when the diffusion-gradient was applied along the foot-head orientation. Subject 3 is characterised by a marked increase in the average tissue velocity, indicative of increased subject motion. $V(t)$ maps estimated from the b_{100} velocity profiles (Figures S9–S11). Note that no coronal data were acquired in Subject 1, as described in Section 3. **Table S1:** Initialisation parameters and bounds for simulated data fitting. **Table S2:** Sequence parameters for supporting acquisitions. T_1 map estimated from the ep2d_se data assuming monoexponential signal evolution (custom code). T_2 map estimated from the se_mc data using via an EPG model (custom code), as described in Tendler et al. B_1 map estimated from 3DREAM sequence provided by automated scanner reconstruction. The DW-SE EPI data were first downsampled to the equivalent resolution of the DW-SSFP data (32×32), with diffusion coefficients subsequently estimated for each diffusion gradient orientation and reconstructed into a tensor using custom code. Datasets were coregistered to the DW-SSFP data prior to processing using FLIRT. **Table S3:** Initialisation parameters and bounds for experimental data fitting.